Plasma Phys. Control. Fusion **41** (1999) 1–34. Printed in the UK PII: S0741-3335(99)94727-9

Numerical simulation of ion cyclotron waves in tokamak plasmas

M Brambilla

Max–Planck Institut für Plasmaphysik, EURATOM Association, Garching bei München, Germany

Received 11 September 1998

Abstract. The code TORIC solves the finite Larmor radius wave equations in the ion cyclotron range of frequencies in arbitrary axisymmetric toroidal geometry. The model used, based on the finite Larmor radius approximation, describes the compressional and torsional Alfvén waves and ion Bernstein waves excited by linear mode conversion. Absorption by the ions occurs at the fundamental and first harmonic of the cyclotron frequency, and by the electrons through Landau and transit time damping.

The numerical solution is based on the spectral representation of the wave fields in the poloidal angle ϑ, and cubic finite elements in the radial variable ψ. The spectral approach in the poloidal angle allows us to evaluate in a numerically efficient way the integrals over the particle orbits along magnetic field lines which arise when the high frequency (HF) plasma current is obtained by solving the linearized Vlasov equation; the leading effects of toroidicity on cyclotron absorption and spatial dispersion are also taken into account. The code offers a number of options, which allow us to compare the complete finite Larmor radius model with simpler approximations, such as the widely used order reduction algorithm, which replaces the excitation of ion Bernstein waves with an equivalent power sink.

1. Introduction

Considerable effort has been devoted to the numerical modelling of ion cyclotron waves propagation and absorption in tokamaks. Models in plane-stratified geometry were implemented first, because they involve only the solution of ordinary differential equations [1–5]. They give useful information on the distribution of the absorbed power among different species in the plasma, and on the efficiency of mode conversion to ion Bernstein waves; moreover, they are particularly appropriate for the evaluation of the antenna load. Only full-wave solutions of Maxwell–Vlasov equations in toroidal geometry [6–15], on the other hand, provide reliable power deposition profiles for comparison with the results of heating and current drive experiments, and allow us to investigate specific effects of toroidicity on wave absorption and mode conversion. A satisfactory model must describe the compressional and torsional Alfvén waves (or, depending on the parallel phase velocity, the kinetic counterpart of the latter), and the lowest order ion Bernstein (IB) waves which can be excited by mode conversion near first-harmonic cyclotron resonances or ion–ion hybrid resonances. Dissipative effects must include absorption by the ions at the cyclotron frequency and its first harmonic, and by the electrons through Landau and transit time damping [16]. Here we describe a new version of the toroidal full-wave code first presented in [10], which has been completely rewritten and renamed TORIC.

0741-3335/99/010001+34$19.50

The first step in the development of a toroidal full-wave code is to write an adequate set of wave equations in the ion cyclotron (IC) frequency range in a hot, inhomogeneous plasma. This is by no means a trivial task, except in the 'cold-plasma' limit, in which the local cold-plasma dielectric tensor is sufficient to describe the plasma response even if the equilibrium is non-homogeneous in space. The cold-plasma approximation, however, is not satisfactory, since it misses IC harmonic damping near $\omega = 2\Omega_{ci}$ and mode conversion to IB waves, which are both finite pressure effects. When finite-temperature effects are important, the high frequency (HF) current in the plasma must be obtained by solving the linearized Vlasov equation; if the equilibrium is non-uniform, this leads, in principle, to a constitutive relation in integro-differential form. In other words, the HF current is a non-local functional of the HF field. In the direction perpendicular to the static magnetic field a substantial simplification can be obtained by expanding in the Larmor radius of the particles, assumed to be much smaller than the perpendicular wavelengths involved. TORIC solves the finite Larmor radius (FLR) wave equations in the approximation derived by Swanson [17] and by Colestock and Kashuba [18] for the ions, augmented by the appropriate FLR terms for the electrons [19]. The Swanson, Colestock and Kashuba (SCK) wave equations, strictly speaking, do not systematically include all second-order terms in the Larmor radius expansion. We will argue in section 3, however, that the terms omitted are quantitatively relevant only for parameters such that the FLR expansion is anyhow invalid (in particular near fundamental ion cyclotron resonances), and that, as a consequence, keeping these terms often leads to non-physical results. The local dispersion relation corresponding to the SCK approximation, by contrast, can be shown to be always a good approximation to the full hot-plasma dispersion relation, even outside the validity range of the FLR expansion, so that problems connected with the breakdown of the FLR expansion in parts of the integration domain can be more easily avoided in practice.

Wave equations of the SCK model where originally obtained assuming for simplicity a plane-stratified geometry with straight static magnetic field. To generalize them to the tokamak case, we have written the HF plasma current obtained in this way in vector form, and then transformed it to toroidal coordinates. In this geometry, however, there is a further complication, due to the fact that the expansion in the Larmor radius puts the constitutive relation into differential form only in directions perpendicular to the static magnetic field: when $\boldsymbol{B}_0 \cdot \boldsymbol{\nabla} B_0 \neq 0$, the relation between HF current and field remains non-local along magnetic field lines. A correct treatment of the resulting integral operators in the wave equations turns out to be important to describe the effects of toroidicity on resonant IC absorption. Our approach to this end will be described in section 5. Writing the HF current in vector form also makes it easy to evaluate the parallel component of the electric field on the same footing as the perpendicular components, rather than iteratively as in [10]. This improves the accuracy of the evaluation of power absorption by the electrons, as required, in particular, for a reliable evaluation of the efficiency of current drive by HF waves in the IC frequency range [20].

The numerical discretization is based on the representation of the solution as a truncated Fourier series in the poloidal angle ϑ, and uses cubic finite elements [21] in the radial variable ψ. The latter have excellent convergence properties, due to the fact that both the electric and magnetic field are continuous at each point of the mesh. Because of the sharp poloidal variation of the coefficients of the wave equations in the IC frequency range, on the other hand, coupling between different poloidal Fourier modes is very strong, and can by no means be regarded as a perturbative effect (in contrast, for example, to the situation in the low-frequency magnetohydrodynamic (MHD) limit). As a consequence, the number of modes required to reach convergence can be quite large, particularly in scenarios with weak absorption. The spectral representation of the wave fields is nevertheless very useful, because it allows a

quantitatively accurate approximation of the integrals along particle orbits which describe the effects of toroidicity on parallel dispersion and collisionless IC absorption.

To facilitate comparison of fully toroidal results with simpler models, a number of options have been added to TORIC. Particularly useful is the implementation of the order reduction algorithm (ORA) [22], which replaces the excitation of ion Bernstein waves by an equivalent power sink. Although based on an euristic approach, the power deposition profiles obtained in this way are quite accurate; the suppression of short wavelength features in the solution, on the other hand, allows relatively coarse meshes to be used both in the poloidal and the radial directions. The resulting reduction in execution time and memory requirements make the ORA option of TORIC a useful tool for routine analysis of IC heating, possibly in conjunction with other codes, such as those describing radial transport in tokamaks.

The paper is organized as follows. In section 2 we describe the plasma configuration, and in section 3 we present the wave equations of the SCK model. In section 4 these equations are put into the Galerkin variational form, which is the basis of the finite elements discretization. In section 5 we introduce the spectral representation of the solution, and discuss our treatment of the integral operators which arise from the integration of the linearized Vlasov equation in toroidal geometry. The regularity conditions at the magnetic axis, and the boundary conditions at the plasma edge, at the antenna and at the Faraday shield, are discussed in section 6. Section 7 is devoted to the power balance. Damping of ion Bernstein waves and collisional broadening of Alfvén resonances are also discussed in this section. The order reduction algorithm is presented in section 8. Section 9 summarizes the numerical implementation. Finally, a few examples are presented in section 10. They include some detailed comparison of the TORIC results with those of the ORA approximation, and those of the code FELICE, which solves the same equations in plane-stratified geometry.

2. Equilibrium model.

2.1. The MHD configuration

The code uses toroidal coordinates ψ, ϑ, φ, where the dimensionless variable ψ labels magnetic surfaces, while ϑ and φ are the poloidal and toroidal angles, respectively. The axisymmetric MHD equilibrium is assumed to have a representation of the form

$$X = X(\psi, \vartheta) \qquad Z = Z(\psi, \vartheta) \tag{1}$$

where X, Z are horizontal and vertical Cartesian coordinates in the poloidal cross section, with origin at a distance R_0 from the vertical axis (the centre of the vacuum vessel). Thus $R = R_0 + X$, $\phi = -\varphi$, Z constitute a cylindrical coordinate system. The covariant metric of the magnetic coordinates can be written

$$g_{ij} = \begin{pmatrix} N_\psi^2 & G & 0 \\ G & N_\tau^2 & 0 \\ 0 & 0 & R^2 \end{pmatrix} \tag{2}$$

with elements

$$\begin{aligned} N_\tau^2 &= \left(\frac{\partial X}{\partial \vartheta}\right)^2 + \left(\frac{\partial Z}{\partial \vartheta}\right)^2 \\ G &= \left(\frac{\partial X}{\partial \psi}\right)\left(\frac{\partial X}{\partial \vartheta}\right) + \left(\frac{\partial Z}{\partial \psi}\right)\left(\frac{\partial Z}{\partial \vartheta}\right) \\ N_\psi^2 &= \left(\frac{\partial X}{\partial \psi}\right)^2 + \left(\frac{\partial Z}{\partial \psi}\right)^2 \end{aligned} \tag{3}$$

satisfying the identity $N_\psi^2 N_\tau^2 = J_\mathrm{p}^2 + G^2$, where J_p is the Jacobian of equations (1)

$$J_\mathrm{p} = \left(\frac{\partial X}{\partial \psi}\right)\left(\frac{\partial Z}{\partial \vartheta}\right) - \left(\frac{\partial Z}{\partial \psi}\right)\left(\frac{\partial X}{\partial \vartheta}\right). \tag{4}$$

In general, ψ and ϑ are not orthogonal, i.e. $G \neq 0$. Orthogonal unit vectors $\boldsymbol{u}_\psi$, $\boldsymbol{u}_\tau$, $\boldsymbol{u}_\varphi$ can nevertheless be defined at each point through

$$\begin{aligned}
\boldsymbol{u}_\psi &= \frac{1}{N_\tau}\left(\frac{\partial Z}{\partial \vartheta}\boldsymbol{u}_X - \frac{\partial X}{\partial \vartheta}\boldsymbol{u}_Z\right) = \frac{J_\mathrm{p}}{N_\tau}\boldsymbol{\nabla}\psi \\
\boldsymbol{u}_\tau &= \frac{1}{N_\tau}\left(\frac{\partial X}{\partial \vartheta}\boldsymbol{u}_X + \frac{\partial Z}{\partial \vartheta}\boldsymbol{u}_Z\right) = N_\tau\left(\boldsymbol{\nabla}\vartheta + \frac{G}{N_\tau^2}\boldsymbol{\nabla}\psi\right) \\
\boldsymbol{u}_\varphi &= R\boldsymbol{\nabla}\varphi
\end{aligned} \tag{5}$$

where $\boldsymbol{u}_X$ and $\boldsymbol{u}_Z$ are unit vectors of the Cartesian coordinates in the poloidal cross section. The static magnetic field has contravariant and physical representations

$$\begin{aligned}
\boldsymbol{B} &= B_0 R_0\{a\, f(\psi)\boldsymbol{\nabla}\varphi \times \boldsymbol{\nabla}\psi + g(\psi)\boldsymbol{\nabla}\varphi\} \\
&= \frac{R_0}{R} B_0(\sin\Theta \boldsymbol{u}_\tau + \cos\Theta \boldsymbol{u}_\varphi)
\end{aligned} \tag{6}$$

respectively, with

$$\tan\Theta(\psi, \vartheta) = \frac{B_\tau}{B_\varphi} = a\frac{N_\tau}{J_\mathrm{p}}\frac{f(\psi)}{g(\psi)}. \tag{7}$$

In principle, the code can easily be interfaced with any tokamak equilibrium solver giving the functions (1) (or the inverse functions $\psi(X, Z)$, $\vartheta(X, Z)$) and $\tan\Theta$ in twice continuous differentiable form. As a default, however, an *approximate* equilibrium is provided, assuming

$$\begin{aligned}
X(\psi, \vartheta) &= \Delta(\psi) + a\psi\cos(\vartheta - \delta(\psi)\sin\vartheta) \\
Z(\psi, \vartheta) &= a\eta(\psi)\sin\vartheta
\end{aligned} \tag{8}$$

where the functions $\Delta(\psi)$ (Shafranov shift), $\eta(\psi)$ (ellipticity) and $\delta(\psi)$ (triangularity) are low-order polynomials inside the separatrix, and are continuously extrapolated to their value at the wall outside it. The dependence of $R\,B_\varphi$ on ψ, which is a finite-β effect, is neglected, i.e. $g(\psi) \equiv 1$, while $f(\psi)$ is determined from Faraday law

$$f(\psi) = \frac{4\pi}{c}\frac{I(\psi)}{R_0 a\, B_0 \int_0^{2\pi}(N_\tau^2/RJ_\mathrm{p})\,\mathrm{d}\vartheta} \tag{9}$$

where $I(\psi)$ is the total toroidal current inside the magnetic surface ψ.

2.2. Differential operators

The numerical approach based on the Galerkin weak-variational formulation requires only first-order differential operators. In terms of the physical components E_ψ, E_τ, E_φ with respect to the local basis (5) the divergence and curl operator are

$$\boldsymbol{\nabla}\cdot\boldsymbol{E} = \frac{1}{RJ_\mathrm{p}}\left\{\frac{\partial}{\partial\psi}(RN_\tau E_\psi) + \frac{\partial}{\partial\vartheta}\left(\frac{R}{N_\tau}(J_\mathrm{p}E_\tau - GE_\psi)\right)\right\} + \frac{1}{R}\frac{\partial E_\varphi}{\partial\varphi} \tag{10}$$

and

$$\begin{aligned}
\boldsymbol{\nabla}\times\boldsymbol{E} = {} & \frac{1}{R}\left\{\frac{1}{N_\tau}\frac{\partial(RE_\varphi)}{\vartheta} - \frac{\partial E_\tau}{\partial\varphi}\right\}\boldsymbol{u}_\psi \\
& + \frac{1}{R}\left\{\frac{\partial E_\psi}{\partial\varphi} - \frac{N_\tau}{J_\mathrm{p}}\left(\frac{\partial(RE_\varphi)}{\partial\psi} - \frac{G}{N_\tau^2}\frac{\partial(RE_\varphi)}{\partial\vartheta}\right)\right\}\boldsymbol{u}_\tau \\
& + \frac{1}{J_\mathrm{p}}\left\{\frac{\partial(N_\tau E_\tau)}{\partial\psi} - \frac{\partial}{\partial\vartheta}\left(\frac{1}{N_\tau}(J_\mathrm{p}E_\psi + GE_\tau)\right)\right\}\boldsymbol{u}_\varphi
\end{aligned} \tag{11}$$

respectively. The HF current in the plasma, on the other hand, is naturally written in the local 'Stix' frame, whose basis unit vectors are related to those of the flux coordinates by

$$\begin{aligned} \boldsymbol{u}_\xi &= \boldsymbol{u}_\psi \\ \boldsymbol{u}_\eta &= \cos\Theta \boldsymbol{u}_\tau - \sin\Theta \boldsymbol{u}_\varphi \\ \boldsymbol{u}_\zeta &= \sin\Theta \boldsymbol{u}_\tau + \cos\Theta \boldsymbol{u}_\varphi. \end{aligned} \tag{12}$$

Here $\boldsymbol{u}_\zeta = \boldsymbol{B}/B$ is the unit vector tangential to the magnetic field line, while $\boldsymbol{u}_\eta$ is orthogonal to it and lies in the magnetic surface. The code works with physical components in this frame, namely

$$\begin{aligned} E_\xi &= E_\psi \\ E_\eta &= \cos\Theta E_\tau - \sin\Theta E_\varphi \\ E_\zeta &= \sin\Theta E_\tau + \cos\Theta E_\varphi. \end{aligned} \tag{13}$$

Although using contravariant components in the global ψ, ϑ, φ coordinates would spare some overhead in the discretization of the system, choice (13) has the advantage of keeping well separated the parallel and perpendicular plasma response, which are different by orders of magnitude, $|E_\zeta| \ll |E_\perp|$.

To represent the HF currents in the plasma we will also need a basis for circularly polarized components perpendicular to $\boldsymbol{B}$. The appropriate definitions in toroidal geometry are

$$\boldsymbol{u}_\pm = \frac{1}{\sqrt{2}}\{\mathrm{e}^{\mp \mathrm{i}\tau}(\boldsymbol{u}_\psi \mp \mathrm{i}\boldsymbol{u}_\eta)\} \qquad E_\pm = \frac{1}{\sqrt{2}}\{\mathrm{e}^{\pm \mathrm{i}\tau}(E_\psi \pm \mathrm{i}E_\eta)\} \tag{14}$$

where

$$\mathrm{e}^{\pm \mathrm{i}\tau} = \frac{1}{\kappa N_\tau}\left(\frac{\partial Z}{\partial \vartheta} \mp \mathrm{i}\cos\Theta \frac{\partial X}{\partial \vartheta}\right) \qquad \kappa^2 = 1 - \frac{\sin^2\Theta}{N_\tau^2}\left(\frac{\partial X}{\partial \vartheta}\right)^2. \tag{15}$$

The coefficients $\mathrm{e}^{\pm \mathrm{i}\tau}$ ensure that $E_\pm$ are uniquely defined also on the magnetic axis.

3. The wave equations in the plasma

3.1. The Swanson–Colestock–Kashuba approximation

Maxwell equations in the plasma can be written

$$\boldsymbol{\nabla} \times \boldsymbol{\nabla} \times \boldsymbol{E} = \frac{\omega^2}{c^2}\left(\boldsymbol{E} + \frac{4\pi \mathrm{i}}{\omega}\boldsymbol{J}^{\mathrm{P}}\right) \tag{16}$$

where $\boldsymbol{J}^{\mathrm{P}}$ is the HF plasma current, which is evaluated by solving the linearized Vlasov equation, and is, in principle, an integral functional of the wave electric field $\boldsymbol{E}$. In the ion cyclotron range of frequencies it is justified to use the small Larmor radius approximation for $\boldsymbol{J}^{\mathrm{P}}$

$$\boldsymbol{J}^{\mathrm{P}} = \boldsymbol{J}^{(0)} + \boldsymbol{J}^{(2)} \tag{17}$$

where suffixes denote the order in the finite Larmor radius (FLR) expansion. To this order $\boldsymbol{J}^{\mathrm{P}}$ has recently been derived [23] directly in axisymmetric toroidal geometry. Here we have followed a somewhat different procedure, starting from the results of [19], in which the Vlasov equation is solved in plane-stratified geometry, and assuming that the vector form of $\boldsymbol{J}^{\mathrm{P}}$ obtained in this limit holds also in toroidal geometry. In the small Larmor radius approximation the role of toroidicity in $\boldsymbol{J}^{\mathrm{P}}$ is critical (i.e. it does not reduce to a simple change of coordinates) only in the integrals over the particle motion along magnetic field lines. In [19] these integrals, which describe parallel dispersion and collisionless absorption, have been treated in a formal way which can be easily extended to the toroidal situation, while they have been completely ignored in [23]. We will discuss their evaluation in section 5.2.

3.1.1. The zero Larmor radius plasma current. The zero Larmor radius plasma current $\boldsymbol{J}^{(0)}$, combined for convenience with the vacuum displacement current, can be written

$$\begin{aligned}\boldsymbol{E} + \frac{4\pi\mathrm{i}}{\omega}\boldsymbol{J}^{(0)} &= \hat{L}E_+\boldsymbol{u}_+ + \hat{R}E_-\boldsymbol{u}_- + \hat{P}E_\zeta\boldsymbol{u}_\zeta \\ &= (\hat{S}E_\psi - \mathrm{i}\hat{D}E_\eta)\boldsymbol{u}_\psi + (\mathrm{i}\hat{D}E_\psi + \hat{S}E_\eta)\boldsymbol{u}_\eta + \hat{P}E_\zeta\boldsymbol{u}_\zeta \end{aligned} \tag{18}$$

where we have introduced the integral operators

$$\begin{aligned}\hat{L}E_+ &= E_+(\boldsymbol{r}) - \sum_\alpha \frac{\omega_{\mathrm{p}\alpha}^2}{\omega^2}\int_{-\infty}^{+\infty}\mathrm{d}u\frac{\mathrm{e}^{-u^2}}{\sqrt{\pi}}\left(-\mathrm{i}\omega\int_{-\infty}^{t}\mathrm{d}t'\,\mathrm{e}^{\mathrm{i}\int_{t'}^{t}(\omega-\Omega_g')\,\mathrm{d}\tau}E_+'\right) \\ \hat{R}E_- &= E_-(\boldsymbol{r}) - \sum_\alpha \frac{\omega_{\mathrm{p}\alpha}^2}{\omega^2}\int_{-\infty}^{+\infty}\mathrm{d}u\frac{\mathrm{e}^{-u^2}}{\sqrt{\pi}}\left(-\mathrm{i}\omega\int_{-\infty}^{t}\mathrm{d}t'\,\mathrm{e}^{\mathrm{i}\int_{t'}^{t}(\omega-\Omega_g')\,\mathrm{d}\tau}E_-'\right) \\ \hat{P}E_z &= E_z(\boldsymbol{r}) - \sum_\alpha \frac{\omega_{\mathrm{p}\alpha}^2}{\omega^2}\int_{-\infty}^{+\infty}\mathrm{d}u\frac{\mathrm{e}^{-u^2}}{\sqrt{\pi}}(2u^2)\left(-\mathrm{i}\omega\int_{-\infty}^{t}\mathrm{d}t'\,\mathrm{e}^{\mathrm{i}\omega(t-t')}E_z'\right)\end{aligned} \tag{19}$$

and

$$\hat{S} = \tfrac{1}{2}(\hat{R} + \hat{L}) \qquad \hat{D} = \tfrac{1}{2}(\hat{R} - \hat{L}). \tag{20}$$

The t'-integrations are along magnetic field lines, with, for each species

$$\boldsymbol{E}' = \boldsymbol{E}\left(\boldsymbol{r} - \int_{t'}^{t}(v_\parallel\boldsymbol{u}_\zeta)\,\mathrm{d}\tau\right) \tag{21}$$

and $u = v_\parallel/v_{\mathrm{th}}$, where $v_{\mathrm{th}} = \sqrt{2T/m}$ is the thermal speed.

3.1.2. The ion FLR current. In the Swansion–Colestock–Kashuba (SCK) approximation [17, 18] only the terms resonant at $\omega = 2\Omega_{\mathrm{ci}}$ are retained in the FLR ion current. They can be written in vector form as [19]

$$\begin{aligned}\frac{4\pi\mathrm{i}}{\omega}\boldsymbol{J}^{(2)} = \frac{c^2}{\omega^2}\mathbf{R}\cdot\{&\boldsymbol{\nabla}_\perp(\sigma^{(2)}\boldsymbol{\nabla}_\perp\cdot(\mathbf{R}\cdot\boldsymbol{E}_\perp) - \mathrm{i}\delta^{(2)}\boldsymbol{\nabla}_\perp\cdot(\boldsymbol{u}_\zeta\times\mathbf{R}\cdot\boldsymbol{E}_\perp)) \\ &-(\boldsymbol{u}_\zeta\times\boldsymbol{\nabla}_\perp)(\sigma^{(2)}\boldsymbol{\nabla}_\perp\cdot(\boldsymbol{u}_\zeta\times\mathbf{R}\cdot\boldsymbol{E}_\perp) + \mathrm{i}\delta^{(2)}\boldsymbol{\nabla}_\perp\cdot(\mathbf{R}\cdot\boldsymbol{E}_\perp))\}\end{aligned} \tag{22}$$

where

$$\hat{\sigma}^{(2)} = \frac{\hat{\rho}^{(2)} + \hat{\lambda}^{(2)}}{2} \qquad \hat{\delta}^{(2)} = \frac{\hat{\rho}^{(2)} - \hat{\lambda}^{(2)}}{2} \tag{23}$$

with

$$\begin{aligned}\hat{\lambda}^{(2)}E_+ &= \frac{1}{2}\sum_i\frac{\omega_{\mathrm{pi}}^2}{\Omega_{\mathrm{ci}}^2}\frac{v_{\mathrm{thi}}^2}{c^2}\int_{-\infty}^{+\infty}\mathrm{d}u\frac{\mathrm{e}^{-u^2}}{\sqrt{\pi}}\left(-\mathrm{i}\omega\int_{-\infty}^{t}\mathrm{d}t'\,\mathrm{e}^{\mathrm{i}\int_{t'}^{t}(\omega-2\Omega_g')\,\mathrm{d}\tau}E_+'\right) \\ \hat{\rho}^{(2)}E_- &= \frac{1}{2}\sum_i\frac{\omega_{\mathrm{pi}}^2}{\Omega_{\mathrm{ci}}^2}\frac{v_{\mathrm{thi}}^2}{c^2}\frac{\omega}{\omega+2\Omega_{ci}}E_-.\end{aligned} \tag{24}$$

The matrix $\mathbf{R} = \mathbf{R}^{-1}$ is the reflection matrix with respect to the plane containing $\boldsymbol{B}_0$: with $\boldsymbol{u}_g = \boldsymbol{\nabla}_\perp B_0/|\boldsymbol{\nabla}_\perp B_0|$ it can be written

$$\mathbf{R}\cdot\boldsymbol{E}_\perp = \boldsymbol{E}_\perp - 2\,\boldsymbol{u}_g\times(\boldsymbol{E}_\perp\times\boldsymbol{u}_g). \tag{25}$$

Neglecting terms of order $\Theta(\partial\Theta/\partial\psi)$ and $\Theta(\partial\Theta/\partial\vartheta)$, one finds

$$\begin{aligned}(\mathbf{R}\cdot\boldsymbol{E}_\perp)_\psi &= C_2\,E_\psi + S_2\,E_\eta \\ (\mathbf{R}\cdot\boldsymbol{E}_\perp)_\eta &= S_2\,E_\psi - C_2\,E_\eta\end{aligned} \tag{26}$$

where

$$C_2 = b_\psi^2 - b_\eta^2 \qquad S_2 = -2b_\psi b_\eta \tag{27}$$

with

$$b_\psi = \frac{1}{\kappa N_\tau}\frac{\partial Z}{\partial \vartheta} \qquad b_\eta = \frac{\cos\Theta}{\kappa N_\tau}\frac{\partial X}{\partial \vartheta} \tag{28}$$

κ being defined in equation (14). It is not difficult to check that

$$\mathbf{R}\cdot\boldsymbol{E} \mp \mathrm{i}\boldsymbol{u}_\zeta \times (\mathbf{R}\cdot\boldsymbol{E}) = 2E_\pm \boldsymbol{u}_\pm. \tag{29}$$

Note that $\boldsymbol{J}^{(2)}$ is not rotationally invariant (the direction $\boldsymbol{\nabla}B_0$ being singled out), but satisfies Onsager relations, which are necessary for energy conservation in the absence of dissipative effects (i.e. when Im $\{\lambda^{(2)}\} = 0$).

3.1.3. The electron FLR current. The SCK model must be completed by taking into account the FLR electron current, which consists of two terms

$$\frac{4\pi\mathrm{i}}{\omega}\boldsymbol{J}_e^{(2)} = \frac{4\pi\mathrm{i}}{\omega}(\boldsymbol{J}_{\mathrm{MP}}^{(2)} + \boldsymbol{J}_{\mathrm{MX}}^{(2)}) \tag{30}$$

respectively, associated with magnetic pumping (MP) and mixing MP with electron Landau damping (ELD)

$$\begin{aligned}
\frac{4\pi\mathrm{i}}{\omega}\boldsymbol{J}_{\mathrm{MP}}^{(2)} &= -2\frac{c^2}{\omega^2}\boldsymbol{\nabla}_\perp \times (\hat{\lambda}^{(o)}(\boldsymbol{\nabla}_\perp \times \boldsymbol{E}_\perp)) \\
\frac{4\pi\mathrm{i}}{\omega}\boldsymbol{J}_{\mathrm{MX}}^{(2)} &= \mathrm{i}\frac{c^2}{\omega^2}\{\boldsymbol{\nabla}_\perp \times (\xi^{(o)}(\boldsymbol{u}_\zeta\cdot\boldsymbol{\nabla})\,E_\zeta \boldsymbol{u}_\zeta) + \boldsymbol{u}_\zeta(\boldsymbol{u}_\zeta\cdot\boldsymbol{\nabla})(\xi^{(o)}(\boldsymbol{u}_\zeta\cdot\boldsymbol{\nabla}_\perp\boldsymbol{E}_\perp))\}
\end{aligned} \tag{31}$$

with

$$\begin{aligned}
\hat{\lambda}^{(o)}\boldsymbol{E} &= \frac{1}{2}\frac{\omega_{\mathrm{pe}}^2}{\Omega_{\mathrm{ce}}^2}\frac{v_{\mathrm{the}}^2}{c^2}\int_{-\infty}^{+\infty}\mathrm{d}u\frac{\mathrm{e}^{-u^2}}{\sqrt{\pi}}\left(-\mathrm{i}\omega\int_{-\infty}^{t}\mathrm{d}t'\,\mathrm{e}^{\mathrm{i}\omega(t-t')}\boldsymbol{E}'\right) \\
\hat{\xi}^{(o)}\,E_j &= \frac{1}{2}\frac{\omega_{\mathrm{pe}}^2}{\omega\Omega_{\mathrm{ce}}}\frac{v_{\mathrm{the}}^2}{c^2}\int_{-\infty}^{+\infty}\mathrm{d}u\frac{\mathrm{e}^{-u^2}}{\sqrt{\pi}}\left(\omega^2\frac{\partial}{\partial\omega}\int_{-\infty}^{t}\mathrm{d}t'\,\mathrm{e}^{\mathrm{i}\omega(t-t')}E_j'\right).
\end{aligned} \tag{32}$$

In addition, the electrons contribute the small quantities

$$\hat{\lambda}_e^2 E_+ = \frac{1}{2}\frac{\omega_{\mathrm{pe}}^2}{\Omega_{\mathrm{ce}}^2}\frac{\omega}{\omega+2\Omega_{\mathrm{ce}}}E_+ \qquad \hat{\rho}_{\mathrm{e}}^2 E_- = \frac{1}{2}\frac{\omega_{\mathrm{pe}}^2}{\Omega_{\mathrm{ce}}^2}\frac{v_{\mathrm{the}}^2}{c^2}\frac{\omega}{\omega-2\Omega_{\mathrm{ce}}}E_- \tag{33}$$

to $\hat{\lambda}^2$, $\hat{\rho}^2$, respectively.

We note that in this approximation we have neglected all the 'diamagnetic' contributions to the HF plasma current $\boldsymbol{J}^{\mathrm{P}}$ (i.e. the terms proportional to gradients of the equilibrium density and temperature, which arise because the distribution functions on the right-hand side of the linearized Vlasov equation depend on the position of the guiding centre rather than of the particles). Omitting these terms eliminates the drift branch of the dispersion relation, but has a negligible influence on waves in the IC frequency range. Less obvious is the omission of the FLR ion terms resonant at the fundamental cyclotron frequency. These terms are always small corrections to the zero-Larmor radius current, which is also resonant at $\omega = \Omega_{\mathrm{ci}}$, in contrast to the FLR terms which have been kept, which are resonant near the first harmonic where $\boldsymbol{J}^{(0)}$ remains finite. The superiority of the SCK model over the complete FLR model, however, is best proved by analysis of the local dispersion relation. According to both the exact hot plasma dispersion relation and to the SCK model, the perpendicular wavevector of the ion Bernstein wave diverges as $\omega \to \Omega_{\mathrm{ci}}$ from above; below Ω_{ci} the IB branch is evanescent. By contrast,

the FLR dispersion relation including also the FLR corrections resonant at the fundamental predicts that this wave remains propagative below the ion cyclotron frequency and throughout the MHD frequency domain $\omega \ll \Omega_{ci}$, although with a wavelength shorter than the ion Larmor radius. Near $\omega = \Omega_{ci}$, moreover, the power absorption predicted by the complete FLR model is not positive-definite [24], in contrast with a general result [25] according to which in a Maxwellian plasma P_{abs} is always positive provided that terms explicitly proportional to the gradients of the equilibrium quantities are neglected. In the SCK model the power absorbed by the ions is always positive, as it should be.

4. Weak-variational formulation

4.1. The variational integral in the plasma

The wave equation is put into Galerkin's weak-variational form by multiplying equation (16) scalarly with an arbitrary vector function $\boldsymbol{F}$ belonging to a suitable test function space (defined so that $\boldsymbol{F}$ satisfies the same boundary conditions as $\boldsymbol{E}$), and integrating over the whole plasma volume

$$\int \mathrm{d}V\, \boldsymbol{F}^* \cdot \left\{ -\frac{c^2}{\omega^2}\boldsymbol{\nabla}\times\boldsymbol{\nabla}\times\boldsymbol{E} + \boldsymbol{E} + \frac{4\pi \mathrm{i}}{\omega}(\boldsymbol{J}^{\mathrm{P}} + \boldsymbol{J}^{\mathrm{A}}) \right\} = 0. \tag{34}$$

The second-order operators are then eliminated by partial integration, and the resulting equation is written

$$\mathcal{Q}_{\mathrm{curl}} + \mathcal{Q}_{\mathrm{pl}} + \mathcal{Q}_{\mathrm{ant}} + \mathcal{S}_{\mathrm{curl}} + \mathcal{S}_{\mathrm{pl}} = 0 \tag{35}$$

where $\mathcal{Q}$, $\mathcal{S}$ denote volume and surface integrals, respectively. The latter extend over the plasma surface and any other discontinuity surface. For simplicity, the displacement current is collected with the zero Larmor radius plasma current, as it is done when defining the dielectric tensor of the uniform plasma. Moreover, $\mathcal{Q}_{\mathrm{pl}}$ and $\mathcal{S}_{\mathrm{pl}}$ will be further split into zero- and second-order terms in the Larmor radius expansion

$$\mathcal{Q}_{\mathrm{pl}} = \mathcal{Q}_{\mathrm{pl}}^{(0)} + \sum_{\alpha} \mathcal{Q}_{\mathrm{pl}}^{(2,\alpha)} \qquad \mathcal{S}_{\mathrm{pl}} = \mathcal{S}_{\mathrm{pl}}^{(0)} + \sum_{\alpha} \mathcal{S}_{\mathrm{pl}}^{(2,\alpha)} \tag{36}$$

where the sum is over particle species. We now list all the terms in equation (35) in turn for the region inside the plasma.

4.1.1. The curl contribution. The identity

$$\boldsymbol{F}^* \cdot (\boldsymbol{\nabla}\times(\boldsymbol{\nabla}\times\boldsymbol{E})) = (\boldsymbol{\nabla}\times\boldsymbol{F}^*)\cdot(\boldsymbol{\nabla}\times\boldsymbol{E}) - \boldsymbol{\nabla}\cdot(\boldsymbol{F}^*\times(\boldsymbol{\nabla}\times\boldsymbol{E})) \tag{37}$$

gives

$$\mathcal{Q}_{\mathrm{curl}} = -\frac{c^2}{\omega^2}\int\!\!\int_{Pl} R J_{\mathrm{p}}\{(\boldsymbol{\nabla}\times\boldsymbol{F}^*)\cdot(\boldsymbol{\nabla}\times\boldsymbol{E})\}\,\mathrm{d}\psi\,\mathrm{d}\vartheta \tag{38}$$

and

$$\mathcal{S}_{\mathrm{curl}} = \frac{c^2}{\omega^2}\int_{S_{\mathrm{pl}}} R N_\tau\{\boldsymbol{u}_\psi\cdot(\boldsymbol{F}^*\times(\boldsymbol{\nabla}\times\boldsymbol{E}))\}\,\mathrm{d}\vartheta \tag{39}$$

respectively.

4.1.2. The zero Larmor radius plasma current. The contribution from the zero Larmor radius plasma current, including the vacuum displacement current, is

$$\begin{aligned} Q_{\rm pl}^{(0)} &= \iint R J_{\rm p}\{F_+^*\hat{L}E_+ + F_-^*\hat{R}E_- + F_\zeta^*\hat{P}E_\zeta\}\,{\rm d}\psi\,{\rm d}\vartheta \\ &= \iint R J_{\rm p}\{F_\psi^*(\hat{S}E_\psi - {\rm i}\hat{D}E_\eta) + F_\eta^*({\rm i}\hat{D}E_\psi + \hat{S}E_\eta) + F_\zeta^*\hat{P}E_\zeta\}\,{\rm d}\psi\,{\rm d}\vartheta. \end{aligned} \tag{40}$$

4.1.3. The ion FLR current. After integration by parts, the contribution of the FLR part of the ion current to the variational integral becomes

$$\begin{aligned} Q_{\rm pl}^{(2,{\rm i})} = -\frac{c^2}{\omega^2}\iint_{Pl} R J_{\rm p}\{&\boldsymbol{\nabla}_\perp\cdot(\mathbf{R}\cdot\boldsymbol{F}_\perp^*)(\hat{\sigma}^{(2)}\boldsymbol{\nabla}_\perp\cdot(\mathbf{R}\cdot\boldsymbol{E}'_\perp) - {\rm i}\delta^{(2)}\boldsymbol{\nabla}_\perp\cdot(\boldsymbol{u}_\zeta\times\mathbf{R}\cdot\boldsymbol{E}'_\perp)) \\ &-\boldsymbol{\nabla}_\perp\cdot(\boldsymbol{u}_\zeta\times\mathbf{R}\cdot\boldsymbol{F}_\perp^*)(\hat{\sigma}^{(2)}\boldsymbol{\nabla}_\perp\cdot(\boldsymbol{u}_\zeta\times\mathbf{R}\cdot\boldsymbol{E}'_\perp) \\ &+{\rm i}\hat{\delta}^{(2)}\boldsymbol{\nabla}_\perp\cdot(\mathbf{R}\cdot\boldsymbol{E}'_\perp))\}\,{\rm d}\psi\,{\rm d}\vartheta \end{aligned} \tag{41}$$

and

$$\begin{aligned} \mathcal{S}_{\rm pl}^{(2,{\rm i})} = \frac{c^2}{\omega^2}\int_{S_{\rm pl}} R N_\tau \boldsymbol{u}_\psi\cdot\{&\mathbf{R}\cdot\boldsymbol{F}_\perp^*(\hat{\sigma}_2\boldsymbol{\nabla}_\perp\cdot(\mathbf{R}\cdot\boldsymbol{E}'_\perp) - {\rm i}\delta_2\boldsymbol{\nabla}_\perp\cdot(\boldsymbol{u}_\zeta\times\mathbf{R}\cdot\boldsymbol{E}'_\perp)) \\ &+\boldsymbol{u}_\zeta\times\mathbf{R}\cdot\boldsymbol{F}_\perp^*(\hat{\sigma}_2\boldsymbol{\nabla}_\perp\cdot(\boldsymbol{u}_\zeta\times\mathbf{R}\cdot\boldsymbol{E}'_\perp) + {\rm i}\hat{\delta}_2\boldsymbol{\nabla}_\perp\cdot(\mathbf{R}\cdot\boldsymbol{E}'_\perp))\}\,{\rm d}\vartheta. \end{aligned} \tag{42}$$

4.1.4. The electron FLR current. After integration by parts, the volume contributions of the FLR part of the electron current to the variational integral become

$$\begin{aligned} Q_{\rm MP}^{(2,{\rm e})} &= -2\frac{c^2}{\omega^2}\iint_{Pl} R J_{\rm p}\{(\boldsymbol{\nabla}_\perp\times\boldsymbol{F}_\perp)^*\hat{\lambda}^{(o)}(\boldsymbol{\nabla}_\perp\times\boldsymbol{E}_\perp)\}\,{\rm d}\psi\,{\rm d}\vartheta \\ Q_{\rm MX}^{(2,{\rm e})} &= {\rm i}\frac{c^2}{\omega^2}\iint_{Pl} R J_{\rm p}\{(\boldsymbol{u}_\zeta\cdot(\boldsymbol{\nabla}_\perp\times\boldsymbol{F}_\perp))^*\hat{\xi}^{(o)}(\partial_\zeta E_\zeta) - (\partial_\zeta F_\zeta)^*\hat{\xi}^{(o)}(\boldsymbol{u}_\zeta\cdot(\boldsymbol{\nabla}_\perp\times\boldsymbol{E}_\perp))\} \end{aligned} \tag{43}$$

while the corresponding surface contributions are

$$\begin{aligned} \mathcal{S}_{\rm MP}^{(2,{\rm e})} &= 2\frac{c^2}{\omega^2}\int_{S_{\rm pl}} R N_\tau \boldsymbol{u}_\psi\cdot\{\boldsymbol{F}_\perp^*\times(\hat{\lambda}^{(o)}(\boldsymbol{\nabla}_\perp\times\boldsymbol{E}_\perp)\}\,{\rm d}\vartheta \\ \mathcal{S}_{\rm MX}^{(2,{\rm e})} &= {\rm i}\frac{c^2}{\omega^2}\int_{S_{\rm pl}} R N_\tau\{\boldsymbol{F}_\perp^*\times(\hat{\xi}^{(o)}(\partial_\zeta E_\zeta)\boldsymbol{u}_\zeta)\cdot\boldsymbol{u}_\psi\}. \end{aligned} \tag{44}$$

4.2. The variational integral in vacuum

In the vacuum region between the plasma surface and the wall a somewhat different formulation is required in order to avoid numerical pollution, i.e. numerically generated oscillations on the scale of the radial mesh step. The origin of this problem is well known. The dispersion relation of plane waves satisfying the discretized equations (in the sense of a local, or WKB, approximation) is slightly different from the dispersion relation of the continuous equations, the error in the wavelength of characteristic modes being of the order of the mesh step Δr. The discretized solution, therefore, is reliable only for waves with wavelengths sufficiently larger than Δr. Pollution occurs when an evanescent wave with evanescence length of the order Δr is transformed by the discretization into a propagative wave with a wavelength of the same order.

In vacuum Maxwell's equations admit only two independent solution. In this case, a third-order FEM discretization *always* introduces a third independent wave (if this were not so, the stiffness matrix would be singular). The spurious wave becomes the dominant feature if it happens to be propagative; even if evanescent, and thus not obviously 'visible' in the results, its presence can cause substantial errors when imposing the boundary conditions at the antenna and the plasma surface. Jiang, Wu and Povinelli [26] (later referred to as JWP) have recently shown that the problem can be avoided by casting Maxwell equations in a form which explicitly guarantees that $\boldsymbol{\nabla}\cdot\boldsymbol{E}=0$ will be satisfied by the solution in vacuum (spectrally polluted solutions manifestly violate this condition). In the JWP formulation the variational integral is

$$\mathcal{Q}_{\rm curl}^{\rm vac}+\mathcal{Q}_{\rm ant}+\mathcal{S}_{\rm curl}^{\rm vac}=0 \tag{45}$$

with

$$\begin{aligned}
\mathcal{Q}_{\rm curl}^{\rm vac} &= \int\!\!\int_V RJ_{\rm p}\{\boldsymbol{F}^*\cdot\boldsymbol{E}-\frac{c^2}{\omega^2}((\boldsymbol{\nabla}\times\boldsymbol{F}^*)\cdot(\boldsymbol{\nabla}\times\boldsymbol{E})+(\boldsymbol{\nabla}\cdot\boldsymbol{F}^*)(\boldsymbol{\nabla}\cdot\boldsymbol{E}))\}\,{\rm d}\vartheta\,{\rm d}\psi\\
\mathcal{Q}_{\rm ant} &= \frac{4\pi{\rm i}}{\omega}\int\!\!\int_V RJ_{\rm p}\left\{\boldsymbol{F}^*\cdot\boldsymbol{J}^{\rm ant}-\frac{c^2}{\omega^2}(\boldsymbol{\nabla}\cdot\boldsymbol{F}^*)(\boldsymbol{\nabla}\cdot\boldsymbol{J}^{\rm ant})\right\}{\rm d}\vartheta\,{\rm d}\psi\\
\mathcal{S}_{\rm curl} &= -\frac{c^2}{\omega^2}\int_{S_{\rm pl}} RN_\tau\{\boldsymbol{u}_\psi\cdot(\boldsymbol{F}^*\times(\boldsymbol{\nabla}\times\boldsymbol{E}))\}\,{\rm d}\vartheta.
\end{aligned} \tag{46}$$

In the plasma this formulation would guarantee that the solution satisfies $\boldsymbol{\nabla}\cdot\boldsymbol{D}=0$, but is difficult to implement because of the appearance of second-order derivatives in the variational integrals. Fortunately, it is also not required, since the FLR wave equations have three independent solutions: we have never observed pollution in the plasma region with the TORIC code. Since the variational integral has a different form in vacuum and in the plasma, on the other hand, the two regions must be treated independently, coding explicitly the surface integrals $\mathcal{S}_{\rm curl}$ and $\mathcal{S}_{\rm pl}$ at the plasma–vacuum interface. In the absence of FLR currents in the plasma these conditions impose the continuity of the Poynting flux through this surface. A physical interpretation of the FLR contributions to the surface integrals from the plasma side has been given in [27]; in practice, for realistic values of the plasma pressure at the edge, these terms are negligibly small.

5. The spectral ansatz

5.1. The variational integral in the spectral representation

We now assume a solution of the form

$$E_\alpha = {\rm e}^{{\rm i}n_\varphi\varphi}\sum_{m=-\infty}^{+\infty}E_\alpha^m(n_\varphi;\psi)\,{\rm e}^{{\rm i}m\vartheta}. \tag{47}$$

Because of axisymmetry there is no coupling between different n_φ components; in the following, the argument n_φ will usually be omitted. With this ansatz, using the set of test functions

$$\boldsymbol{F}=\boldsymbol{F}^{(m)}(\psi)\,{\rm e}^{{\rm i}m\vartheta}\,{\rm e}^{{\rm i}n_\varphi\varphi}\qquad -\infty<m<+\infty \tag{48}$$

the Galerkin equations become

$$\begin{aligned}
\sum_{m'}\int\!\!\int & RJ_{\rm p}\,{\rm e}^{{\rm i}(m'-m)\vartheta}(\boldsymbol{F}^{(m)*}(\psi)\cdot\boldsymbol{\mathcal{Q}}^{\rm op}(m,m')\cdot\boldsymbol{E}^{(m')}(\psi))\,{\rm d}\vartheta\,{\rm d}\psi\\
&+\sum_{\psi_s}\sum_{m'}\int RN_\tau\,{\rm e}^{{\rm i}(m'-m)\vartheta}(\boldsymbol{F}^{(m)*}(\psi_s)\cdot\boldsymbol{\mathcal{S}}^{\rm op}(m,m')\cdot\boldsymbol{E}^{(m')}(\psi_s))\,{\rm d}\vartheta\\
&=\frac{4\pi{\rm i}}{\omega}\int\!\!\int RJ_{\rm p}\,{\rm e}^{-{\rm i}m\vartheta}(\boldsymbol{F}^{(m)*}(\psi)\cdot\boldsymbol{J}_{\rm A}(n_\varphi,\psi,\vartheta))\,{\rm d}\vartheta\,{\rm d}\psi
\end{aligned} \tag{49}$$

for each m, where $\boldsymbol{\mathcal{Q}}^{\mathrm{op}}$ is a bilinear operator of the form

$$\begin{aligned}\boldsymbol{F}^{(m)*}(\psi)\cdot\boldsymbol{\mathcal{Q}}^{\mathrm{op}}(m,m')\cdot\boldsymbol{E}^{(m')}(\psi)\\ =\sum_{\alpha}\sum_{\beta}\left\{\frac{\mathrm{d}F_{\alpha}^{m*}}{\mathrm{d}\psi}\Gamma_{\alpha\beta}(m,2;m',2)\frac{\mathrm{d}E_{\beta}^{m'}}{\mathrm{d}\psi}+\frac{\mathrm{d}F_{\alpha}^{m*}}{\mathrm{d}\psi}\Gamma_{\alpha\beta}(m,2;m',1)E_{\beta}^{m'}\right.\\ \left.+F_{\alpha}^{m*}\Gamma_{\alpha\beta}(m,1;m',2)\frac{\mathrm{d}E_{\beta}^{m'}}{\mathrm{d}\psi}+F_{\alpha}^{m*}\Gamma_{\alpha\beta}(m,1;m',1)E_{\beta}^{m'}\right\}.\end{aligned}\tag{50}$$

The operator $\boldsymbol{\mathcal{S}}^{\mathrm{op}}$ has a similar representation, except that it does not contain derivatives of $\boldsymbol{F}^{*}$. The evaluation of the coefficients $\Gamma_{\alpha\beta}$ is lengthy but straightforward, and will be omitted for brevity; a complete list can be found in [28].

The coefficients $\Gamma_{\alpha\beta}$ in equation (49) are functions of both ψ and ϑ. At constant ψ, therefore, equations (48) have the form of a discrete convolution between the Fourier components of the quantities $\Gamma_{\alpha\beta}$ and those of the electric field, weighted with the Jacobian RJ_{p}. Thus, the spectral ansatz transforms the partial differential wave equations into an infinite set of ordinary differential equations, whose coefficients can be efficiently evaluated using the fast Fourier transform (FFT). In numerical implementation, the Fourier expansions must be truncated to include a finite number of terms; this number must be large enough to allow a good reconstruction of the sharp poloidal variation of the coefficients of the plasma current in the presence of cyclotron resonances, and of the short-wavelength ion Bernstein waves in the solution (47). These conditions can be uncomfortably severe, particularly in the outer region of large plasmas; but at least in principle, convergence can be achieved if there is sufficient damping.

5.2. Evaluation of the orbit integrals

An important advantage of the spectral ansatz is that it puts the integral along the parallel trajectories of the particles which appear in equations (19), (24) and (31) into a form which is analytically tractable. Thus, for example, in the zero Larmor radius terms in the plasma current we have

$$\hat{L}E_{+}=\sum_{m'}\hat{L}(\psi,\vartheta;k_{\zeta}^{m'})E_{+}^{m'}\tag{51}$$

with

$$\hat{L}(\psi,\vartheta;k_{\zeta}^{m'})=1-\sum_{\alpha}\frac{\omega_{\mathrm{p}\alpha}^{2}}{\omega^{2}}(-x_{o\alpha}\tilde{Z}(x_{1\alpha})).\tag{52}$$

Here $\tilde{Z}$ is the toroidal plasma dispersion function (TPDF)

$$-x_{o\alpha}\tilde{Z}(x_{n\alpha})=\int_{-\infty}^{+\infty}\mathrm{d}u\,\frac{\mathrm{e}^{-u^{2}}}{\sqrt{\pi}}\left\{-\mathrm{i}\omega\int_{-\infty}^{t}\mathrm{e}^{\mathrm{i}\int_{t'}^{t}k_{\zeta}^{m'}v_{\mathrm{th}}(x_{n\alpha}''-u'')\,\mathrm{d}t''}\,\mathrm{d}t'\right\}\tag{53}$$

with argument

$$x_{n,\alpha}=x_{n,\alpha}(m',\psi,\vartheta)=\frac{\omega-n\Omega_{\mathrm{c}\alpha}}{k_{\zeta}^{m'}v_{\mathrm{th}\alpha}}\tag{54}$$

where

$$k_{\zeta}^{m}(\psi,\vartheta)=k_{\parallel}^{mn_{\varphi}}=\frac{m}{N_{\tau}}\sin\Theta+\frac{n_{\varphi}}{R}\cos\Theta\tag{55}$$

can be regarded as the local parallel component of the wavevector of the m'th Fourier component of the electric field. The operators $\hat{R}$ and $\hat{P}$ can similarly be expressed in terms of the TPDF

of arguments $x_{-1,\alpha}$, $x_{0,\alpha}$, respectively, and the FLR coefficients $\hat{\lambda}^2$ and $\hat{\rho}^2$ can similarly be expressed in terms of the TPDF of argument $x_{\pm 2,\alpha}$.

For large argument, $|x_n| \gg 1$, $\tilde{Z}$ has the same asymptotic behaviour as the Fried-Conte plasma dispersion function of the uniform plasma [29]

$$Z(x_n) = \frac{1}{\sqrt{\pi}} \int_{-\infty}^{+\infty} \frac{\mathrm{e}^{-u^2}}{u - x_n}\, \mathrm{d}u + \mathrm{i}\sqrt{\pi}\, \mathrm{e}^{-x_n^2} \tag{56}$$

to which it reduces exactly in the limit of a uniform magnetic field. In this limit, $\hat{L}$, $\hat{R}$, $\hat{P}$ become the usual expressions for the elements of the plasma dielectric tensor in the zero Larmor radius approximation; similarly, $-k_\perp^2 \hat{\lambda}^2$, $-k_\perp^2 \hat{\rho}^2$, $-k_\perp^2 \hat{\lambda}^o$ and $-k_\perp k_\parallel \hat{\xi}_0$ reproduce the appropriate finite Larmor radius corrections to ϵ. Due to the toroidal inhomogeneity of the static magnetic field, on the other hand, $\tilde{Z}$ differs appreciably from Z in the resonance layer $|x_n| = O(1)$ where spatial dispersion and damping are strong; the most important effect is an appreciable broadening of the width of the resonance domain.

It is also important to note that if the magnetic field has a non-vanishing poloidal component the argument of $\tilde{Z}$ in equation (53) depends explicitly on the poloidal number m': in the Fourier representation each poloidal component of the electric field elicits a different response from the plasma. A practical consequence is that the number of times $\tilde{Z}$ has to be evaluated is very large, and can easily dominate the CPU time consumption unless a very efficient algorithm is used. It is clearly out of question to evaluate the double integral (53) as it stands.

5.3. Approximations of toroidal plasma dispersion functions

The time integral in equation (53) has to be formally evaluated according to the Landau prescription, $\mathrm{Im}\,(\omega) \to 0+$. If this limit is taken literally, however, the TPDF behaves resonantly not only at the harmonics of the cyclotron frequency, but also at the harmonics of the toroidal bounce frequencies of passing and trapped particles [30, 31]. This is not only analytically and numerically untractable, but in most cases also physically incorrect. As discussed by [32], collisional phase diffusion efficiently destroys the phase memory of the particles, thereby eliminating the bounce frequency dependence of the plasma response. Hamiltonian stochasticity induced by repeated resonant wave–particle interactions can also have the same effect [33].

Because of phase diffusion, only the contribution from the last stationary point in the τ integral, i.e. from the last transit through a cyclotron resonance, has to be taken into account in equation (56). The resulting form of the TPDF has been discussed in [34–40]. A thorough treatment is due to Lamalle [38, 39] who has also indicated how to evaluate the velocity integrals for general non-Maxwellian distribution functions. More drastic simplifications, however, are required here to keep the execution time within reasonable limits. A possible approach, based on the assumption that ions cross the resonance layer with constant velocity and that only quadratic terms need to be retained in the expansion of the phase around the stationary point, has been suggested in [35, 36]. Unfortunately, when approximated in this way, the imaginary part of $\tilde{Z}$ is not positive definite. As noted in [37], this gives rise to difficulties in interpreting the power balance, since it makes the local power deposition by ion cyclotron damping negative (plasma 'cooling') in some regions, even if the ion distribution is Maxwellian. Using his more accurate treatment of particle motion, Lamalle [38] has shown that the local power deposition in a Maxwellian plasma is positive defined everywhere, as one would expect.

An accurate approximation of the TPDF which avoids non-physical oscillations of $\mathrm{Im}\,(\tilde{Z})$ in the asymptotic region has been proposed in [41]. Following this reference, in TORIC $\tilde{Z}$ is approximated by the ordinary plasma dispersion function Z with the argument evaluated using

an appropriate 'effective' parallel wavenumber

$$-x_0\tilde{Z}(x_n) \simeq -\bar{x}_0\, Z(\bar{x}_n) \qquad \bar{x}_n = \frac{\omega - n\Omega_c}{(k_\parallel)_{\rm eff}\, v_{\rm th}} \tag{57}$$

where $(k_\parallel)_{\rm eff}$ is given by

$$(k_\parallel)_{\rm eff} \simeq k_\zeta^{m'} \frac{\sqrt{1+4\gamma}-1}{2\gamma} \tag{58}$$

with

$$\gamma \simeq \left(\frac{\omega}{2k_\parallel^2 R_{v\rm th}}\right)\left(-\frac{1}{R}\frac{\partial R}{\partial \vartheta}\right)\sin\Theta \tag{59}$$

evaluated at the cyclotron resonance. This equation can be understood by noting that $L_{\rm res} \simeq (2R_{v_{\rm th}}/n\Omega\sin\Theta)^{1/2}$ is the resonance length for a single ion; the projection of this length in the poloidal plane adds nonlinearly to the thermal Doppler broadening $(k_\parallel v_{\rm th}/\omega)R$ of the cyclotron resonance layer. In particular $(k_\parallel)_{\rm eff}$ remains finite even in the limit $k_\zeta^{m'} \to 0$

$$(k_\parallel)_{\rm eff} \to \left(\frac{\omega}{2Rv_{\rm th}}\sin\Theta\right)^{1/2} \qquad \text{for } k_\parallel \to 0. \tag{60}$$

Equations (58)–(60) take advantage of the efficient algorithms available to evaluate the function Z [42].

6. Boundary conditions in the spectral representation

6.1. Regularity conditions on the magnetic axis

The Cartesian components of $\boldsymbol{E}$ on the magnetic axis must be independent from ϑ

$$\begin{aligned} E_X(0) &= \left(\frac{1}{N_\tau}\frac{\partial Z}{\partial\vartheta}\right)_0 E_\psi(0,\vartheta) + \left(\frac{1}{N_\tau}\frac{\partial X}{\partial\vartheta}\right)_0 E_\eta(0,\vartheta) \\ E_Z(0) &= -\left(\frac{1}{N_\tau}\frac{\partial X}{\partial\vartheta}\right)_0 E_\psi(0,\vartheta) + \left(\frac{1}{N_\tau}\frac{\partial Z}{\partial\vartheta}\right)_0 E_\eta(0,\vartheta). \end{aligned} \tag{61}$$

This completely defines the harmonic contents of the electric field components at $\psi = 0$. It is convenient to write the resulting conditions in rotating components. Defining

$$\left(\frac{1}{N_\tau}\frac{\partial Z}{\partial\vartheta}\right)_0 = \sum_m Z^m\, {\rm e}^{{\rm i}m\vartheta} \qquad \left(\frac{1}{N_\tau}\frac{\partial Z}{\partial\vartheta}\right)_0 = \sum_m X^m\, {\rm e}^{{\rm i}m\vartheta} \tag{62}$$

we obtain

$$\begin{aligned} 0 &= \sum_{m'} (Z^{(m-m')} \mp {\rm i}X^{(m-m')})(E_\psi^{(m')}(0) \pm {\rm i}E_\eta^{(m')}(0)) \\ 0 &= E_\zeta^{(m)}(0) \end{aligned} \tag{63}$$

for all $m \neq 0$. If magnetic surfaces approach circular shape as $\psi \to 0$, then $X^{-1} = -X^1 = i/2$, $Z^{-1} = Z^1 = 1/2$, and all other coefficients vanish. Equations (63) then reduces to

$$E_\psi^1 + {\rm i}E_\eta^1 = 0 \qquad E_\psi^{-1} - {\rm i}E_\eta^{-1} = 0 \qquad E_\psi^m = E_\eta^m \equiv 0 \qquad \text{for all other } m \tag{64}$$

These conditions suffice to guarantee that the differential operators $\boldsymbol{\nabla}\cdot\boldsymbol{E}$ and $\boldsymbol{\nabla}\times\boldsymbol{E}$ (hence the wave magnetic field $\boldsymbol{B}$) remain finite on the magnetic axis. Additional conditions on the derivatives, which we omit for brevity, should in principle be imposed to ensure that $\boldsymbol{B}$ and $\boldsymbol{\nabla}\cdot\boldsymbol{E}$ are also independent from ϑ at $\psi = 0$. These conditions, however, are enforced

numerically to a good approximation by the divergent behaviour of the appropriate elements of the metrics for $\psi \to 0$. As a consequence, it makes almost no difference whether the additional conditions are explicitly taken into account or not (both options are available in the code).

6.2. Boundary conditions at the plasma edge

To implement the boundary conditions required by the different forms of variational integrals in plasma and in vacuum, the plasma–vacuum interface is represented in the radial mesh by two coincident points, representing its plasma and vacuum side, respectively. On each side the appropriate surface contribution is added to the matrix of the discretized system (cf equations (49) and (50)), expressed in terms of the field components on the other side of the same surface. This gives two natural boundary conditions, which ensure the continuity of the power flux through the plasma surface. In addition, the continuity of the components of the electric field tangential to this surface must be separately imposed

$$E^m_\eta|_{\rm p} = E^m_\eta|_v \qquad E^m_\zeta|_{\rm p} = E^m_\zeta|_v \tag{65}$$

for each poloidal Fourier component.

6.3. Boundary conditions at the Faraday shield, the antenna, and the wall

The Faraday screen is modelled by imposing

$$\begin{aligned}&\cos(\Theta-\alpha_{\rm F})(E^m_\eta|_{\rm p} - E^m_\eta|_v) - \sin(\Theta-\alpha_{\rm F})(E^m_\zeta|_{\rm p} - E^m_\zeta|_v) = 0\\ &\sin(\Theta-\alpha_{\rm F})E^m_\eta|_{\rm p} + \cos(\Theta-\alpha_{\rm F})E^m_\zeta|_{\rm p} = \sin(\Theta-\alpha_{\rm F})E^m_\eta|_v + \cos(\Theta-\alpha_{\rm F})E^m_\zeta|_v = 0\end{aligned} \tag{66}$$

at $\psi = \psi_{\rm FS}$, where $\alpha_{\rm F}$ is the inclination of the screen blades to the horizontal (toroidal) direction. Often the surface $\psi = \psi_{\rm FS}$ is taken to coincide with the plasma surface, in which case equations (66) simply replace conditions (65).

The antenna is modelled by a current sheath

$$\boldsymbol{J}^{\rm A} = \frac{N_\tau}{J_{\rm p}} \sum_{n_\varphi} J^{\rm s}(\vartheta)\, {\rm e}^{{\rm i}n_\varphi \varphi} \delta(\psi-\psi_{\rm A})(\cos(\Theta-\alpha_{\rm A})\boldsymbol{u}_\eta + \sin(\Theta-\alpha_{\rm A})\boldsymbol{u}_\zeta) \tag{67}$$

at the surface $\psi = \psi_{\rm A}$, where $J^{\rm s}$ is a line current density (A m^{-1}), and $\pi/2 + \alpha_{\rm A}$ is the angle made by the antenna conductors with the static magnetic field. The wave magnetic field tangent to the surface $\psi = \psi_{\rm A}$ is then discontinuous, and the jump conditions (67) for the tangential HF magnetic field in the spectral representation give the two natural boundary conditions

$$\begin{aligned}&\frac{c^2}{\omega^2}\sum_{m'}\int RN_\tau\, {\rm e}^{{\rm i}(m'-m)\vartheta}((\boldsymbol{\nabla}\times\boldsymbol{E}^{m'})_\zeta)_{\psi=\psi_{\rm A}} = \frac{4\pi{\rm i}}{\omega}\int RN_\tau\, {\rm e}^{-{\rm i}m\vartheta} J^{\rm s}(\vartheta, n_\varphi)\cos(\Theta-\alpha)\,{\rm d}\vartheta\\ &\frac{c^2}{\omega^2}\sum_{m'}\int RN_\tau\, {\rm e}^{{\rm i}(m'-m)\vartheta}((\boldsymbol{\nabla}\times\boldsymbol{E}^{m'})_\eta)_{\psi=\psi_{\rm A}} = -\frac{4\pi{\rm i}}{\omega}\int RN_\tau\, {\rm e}^{-{\rm i}m\vartheta} J^{\rm s}(\vartheta, n_\varphi)\sin(\Theta-\alpha)\,{\rm d}\vartheta\end{aligned} \tag{68}$$

which are manifestly equivalent to the condition

$$[\mathcal{S}_{\rm curl}]_{\psi_{\rm A}} = \mathcal{Q}_{\rm ant} \tag{69}$$

The right-hand side of equation (60) is the forcing term of the whole system. In addition, we must require continuity of the parallel electric field across the surface of the antenna

$$[E^m_\eta]_{\psi_{\rm A}} = 0 \qquad [E^m_\zeta]_{\psi_{\rm A}} = 0 \tag{70}$$

for all m. Except for the forcing term, the conditions at the antenna are identical in structure to those at the plasma edge, and are imposed in the same way.

Finally, the conditions at the metallic wall translate into

$$E_\eta^m(1) = E_\zeta^m(1) = 0 \tag{71}$$

again for all m.

7. The power balance

7.1. The local power balance in the spectral representation

Identifying in equation (52) $\boldsymbol{F}$ with $\boldsymbol{E}$ and taking the imaginary part, we obtain

$$-\mathrm{Re}\sum_m \left\{ \iint R J_\mathrm{p}\, \mathrm{e}^{-\mathrm{i}m\vartheta} (\boldsymbol{E}^{(m)*}(\psi)\cdot \boldsymbol{J}_\mathrm{A}(n_\varphi,\psi,\vartheta))\,\mathrm{d}\vartheta\,\mathrm{d}\psi \right\}$$
$$= \frac{\omega}{4\pi}\mathrm{Im}\sum_m\sum_{m'}\left\{ \iint R J_\mathrm{p}\, \mathrm{e}^{\mathrm{i}(m'-m)\vartheta} (\boldsymbol{E}^{(m)*}(\psi)\cdot \boldsymbol{\mathcal{Q}}^\mathrm{op}\cdot \boldsymbol{E}^{(m')}(\psi))\,\mathrm{d}\vartheta\,\mathrm{d}\psi \right\}. \tag{72}$$

This is an exact consequence of Vlasov–Maxwell equations. The left-hand side is the power launched by the antenna, but the integrand of the right-hand side differs from the local rate of dissipation by the divergence of a vector which represents a reversible transport of oscillation energy by the hot plasma waves. This difference averages to zero on each magnetic surface. The concept of irreversible HF power dissipation, moreover, is meaningful only for times much longer than the average collision time, and therefore typically also than the transit time of thermal particles in the tokamak. Hence, it will suffice to consider the local dissipation rate averaged on each magnetic surface, whose form has been discussed in [25] (we recall that the difference between $P_\mathrm{abs}(\psi)$ and the integrand of equation (72) is the divergence of the kinetic power flux). We now enumerate the various contributions to $P_\mathrm{abs}(\psi)$.

7.1.1. Fundamental ion cyclotron absorption. According to [25] we can write P_i^1 in two equivalent ways

$$P_\mathrm{i}^1(\psi) = \frac{\omega}{8\pi}\sum_m\sum_{m'}\int R J_\mathrm{p}\, \mathrm{e}^{\mathrm{i}(m'-m)\vartheta}\{E_+^{(m)*}(\psi)\{\mathrm{Im}\,(L(\psi,\vartheta,k_\zeta^{m'}))$$
$$+\mathrm{Im}\,(L(\psi,\vartheta,k_\zeta^{m}))\}E_+^{(m')}(\psi)\}$$
$$= \frac{\omega}{4\pi}\mathrm{Re}\sum_m\sum_{m'}\int R J_\mathrm{p}\, \mathrm{e}^{\mathrm{i}(m'-m)\vartheta}\{E_+^{(m)*}(\psi)\mathrm{Im}\,(L(\psi,\vartheta,k_\zeta^{m'}))E_+^{(m')}(\psi)\}\,\mathrm{d}\vartheta. \tag{73}$$

The power balance has been implemented in the last, asymmetric form, which is more convenient numerically.

7.1.2. Electron Landau damping.

$$P_\mathrm{e}^0(\psi) = \frac{\omega}{4\pi}\mathrm{Re}\sum_m\sum_{m'}\int R J_\mathrm{p}\, \mathrm{e}^{\mathrm{i}(m'-m)\vartheta}\{E_\zeta^{(m)*}(\psi)\,\mathrm{Im}\,(P(\psi,\vartheta,k_\zeta^{m'}))E_\zeta^{(m')}(\psi)\}\,\mathrm{d}\vartheta. \tag{74}$$

7.1.3. Ion second-harmonic absorption.

$$P_{\rm i}^{(2)}(\psi) = -\frac{\omega}{8\pi}{\rm Re}\sum_{m,m'}\frac{c^2}{\omega^2}\int R J_{\rm p}\,{\rm e}^{{\rm i}(m'-m)\vartheta}\{\boldsymbol{\nabla}_\perp\cdot(\mathbf{R}\cdot\boldsymbol{E}_\perp^m + {\rm i}\boldsymbol{u}_\zeta\times\mathbf{R}\cdot\boldsymbol{E}_\perp^m)^* \times{\rm Im}\,(\hat{\lambda}_{\rm i}^{(2)}(\psi,\vartheta;k_\zeta^{m'}))\cdot\boldsymbol{\nabla}_\perp\cdot(\mathbf{R}\cdot\boldsymbol{E}_\perp^{m'} + {\rm i}\boldsymbol{u}_\zeta\times\mathbf{R}\cdot\boldsymbol{E}_\perp^{m'})\}\,{\rm d}\vartheta. \quad (75)$$

7.1.4. Electron transit time damping.

$$P_{\rm e}^{\rm TT}(\psi) = -\frac{\omega}{4\pi}{\rm Re}\sum_{m,m'}\frac{c^2}{\omega^2}\int R J_{\rm p}\,{\rm e}^{{\rm i}(m'-m)\vartheta}\{(\boldsymbol{\nabla}_\perp\times\boldsymbol{E}_\perp^m)^* \cdot{\rm Im}\,(2\hat{\lambda}^0(\psi,\vartheta;k_\zeta^{m'}))\cdot(\boldsymbol{\nabla}_\perp\times\boldsymbol{E}_\perp^{m'})\,{\rm d}\vartheta. \quad (76)$$

7.1.5. Mixed electron term.

$$P_{\rm e}^{\rm mxd}(\psi) = \frac{\omega}{8\pi}{\rm Re}\sum_{m,m'}\frac{c^2}{\omega^2}\int R J_{\rm p}\,{\rm e}^{{\rm i}(m'-m)\vartheta}\{((\boldsymbol{\nabla}_\perp\times\boldsymbol{E}_\perp^m)^*\cdot\boldsymbol{u}_\zeta)\,{\rm Im}\,(\hat{\xi}_{\rm e}^0(\psi,\vartheta;k_\zeta^{m'}))(k_\zeta^{m'}E_\zeta^{m'}) + (k_\zeta^m E_\zeta^m)^*\cdot{\rm Im}\,(\hat{\xi}_{\rm e}^0(\psi,\vartheta;k_\zeta^{m'}))\cdot((\boldsymbol{\nabla}_\perp\times\boldsymbol{E}_\perp^{m'})\cdot\boldsymbol{u}_\zeta)\}\,{\rm d}\vartheta. \quad (77)$$

7.2. The global power balance

By integrating equations (73)–(77) over the plasma volume, the total power absorbed $P_{\rm abs}$ and its repartition among different species (ion and electrons) is obtained. A consistency check is offered by the fact that the total absorbed power summed over species must be equal to the power radiated by the antenna

$$P_{\rm ant} = \frac{1}{2}{\rm Re}\sum_m E_\eta^{(m)*}(\psi_{\rm A})\cdot\hat{J}_{\rm s}^{(m)} \quad (78)$$

with

$$\hat{J}_{\rm s}^{(m)} = \int R N_\tau\,{\rm e}^{-{\rm i}m\vartheta}J_{\rm s}(\vartheta)\,{\rm d}\vartheta. \quad (79)$$

In addition $P_{\rm abs}$ must be equal to the electromagnetic power flux across the magnetic surface $\psi = \psi_{\rm A}$ toward the plasma centre, which in spectral representation can be written

$$P_{\rm em} = \frac{c}{8\pi}\sum_{m,m'}\int R N_\tau\,{\rm e}^{{\rm i}(m-m')\vartheta}\{\boldsymbol{E}_\perp^{(m)*}\times(\boldsymbol{\nabla}_\perp\times\boldsymbol{E}_\perp^{m'})\cdot\boldsymbol{u}_\psi\}\,{\rm d}\vartheta. \quad (80)$$

Comparison of $P_{\rm abs}$ with both $P_{\rm ant}$ and $P_{\rm em}$ gives an idea of the numerical accuracy of the solution.

7.3. Electron Landau damping of ion Bernstein waves

As ion Bernstein (IB) waves propagate away from the mode-conversion layer, their wavelength decreases rapidly, until the small Larmor radius (FLR) approximation finally breaks down. Using the FLR expansion outside its validity domain leads to numerical difficulties and to physically wrong results. Among the latter is the fact that electron Landau damping (ELD) of IB waves is grossly underestimated as soon as the condition $\lambda_{\rm i} \ll 1$ is violated. In the FLR approximation ELD is largely suppressed by electromagnetic corrections [43]. The internal cancellations in the dispersion relation responsible for this effect, however, hold only to first order in $\lambda_{\rm i}$, so that ELD becomes increasingly important again as the wavelength of IB

waves decreases. To obtain reliable power deposition profiles in mode conversion scenarios, therefore, one must 'correct' the FLR wave equations to take ELD of IB waves into account. It is possible to simulate the amount of ELD predicted by the local dispersion relation, without altering the structure of the wave equations and without affecting damping of the fast wave or the efficiency of mode conversion, by adding an appropriate imaginary part to the FLR coefficient $\sigma^{(2)} = (\lambda^{(2)} + \rho^{(2)})/2$

$$\delta\sigma^{(2)} = -\mathrm{i}\sigma^{(2)} \frac{\mathrm{Im}\,(n_\perp^2|_{\mathrm{IBW}})}{\mathrm{Re}\,(n_\perp^2|_{\mathrm{IBW}})} \qquad \text{if } \mathrm{Re}\,(n_\perp^2|_{\mathrm{IBW}}) > 0 \tag{81}$$

where the imaginary part of $n_\perp^2|_{\mathrm{IBW}}$ is obtained by solving the 'quasi-electrostatic' dispersion relation [43]

$$0 = \sum_i \frac{\omega_{\mathrm{pi}}^2}{\Omega_{\mathrm{ci}}^2}\left(\frac{1 - I_0(\tilde\lambda_{\mathrm{i}})\,\mathrm{e}^{-\tilde\lambda_{\mathrm{i}}}}{\tilde\lambda_{\mathrm{i}}} - 2\sum_{n=1}^{2}\frac{I_n(\tilde\lambda_{\mathrm{i}})\,\mathrm{e}^{-\tilde\lambda_{\mathrm{i}}}}{\tilde\lambda_{\mathrm{i}}}\frac{\varpi^2}{\varpi^2 - n^2}\right) + \frac{n_\parallel^2 P_{\mathrm{e}}}{n_\perp^2 - P_{\mathrm{e}}} \tag{82}$$

with $\tilde\lambda_{\mathrm{i}} = k_\perp^2 v_{\mathrm{thi}}^2/2\Omega_{\mathrm{ci}}^2$, $\varpi_{\mathrm{i}} = \omega/\Omega_{\mathrm{ci}}$, and

$$P_{\mathrm{e}} = -\frac{\omega_{\mathrm{pe}}^2}{\omega^2} x_{0\mathrm{e}}^2 Z'(x_{0\mathrm{e}}). \tag{83}$$

It might at first sight seem non-physical to simulate ELD by modifying the coefficient of a differential operator which acts only on the perpendicular components of the wave electric field. A more natural choice would be to modify $\hat{P}$ or its FLR correction (the corresponding operator is also optionally coded in TORIC, although never important). It is not difficult to see, however, that in this way one would affect mostly electron Landau damping of the compressional wave, which is not the desired effect. It can be shown, on the other hand, that the factor which multiplies $\sigma^{(2)}$ on the right-hand side of equation (81) is essentially the ratio $|E_z/E_x|^2$ for the IB wave, so that the damping introduced is not only affecting this wave, but is actually also proportional to $|E_z|^2$, as one would expect [43].

7.4. Stochastic ion Landau damping of ion Bernstein waves

For low values of the toroidal wavenumber n_φ ELD is too weak (although never entirely vanishing if the poloidal component of $\boldsymbol{B}_0$ is taken into account) to ensure that IB waves are completely damped before reaching the plasma edge. In this case we add to $\sigma^{(2)}$ a correction which simulates the onset of perpendicular ion Landau damping when $k_{\perp\rho_{\mathrm{i}}}$ exceeds a certain value

$$\frac{\delta\sigma^{(2)}}{\sigma^{(2)}} = -\mathrm{i}K_1\left(1 - \frac{\tilde\lambda_{\mathrm{crit}}}{\tilde\lambda_m}\right)^4 \mathrm{e}^{-K_2 x_\perp^2} \qquad \text{if } \tilde\lambda_m > \tilde\lambda_{\mathrm{crit}} \tag{84}$$

where $x_\perp = \omega/k_\perp v_{\mathrm{th}m}$, and K_1, K_2, and $\tilde\lambda_{\mathrm{crit}}$, are parameters which can be adjusted by the user. The $\tilde\lambda_{\mathrm{crit}}$-dependent factor provides a smooth transition between the undamped and the damped region, and makes sure that all damping occurs far from the mode conversion region, and does not interfere with mode conversion itself and with the reflection of the fast wave from the ion–ion cut off.

At high harmonics, $\omega \gg \Omega_{\mathrm{ci}}$, perpendicular ion Landau damping arises due to the onset of Hamiltonian stochasticity in the ion motion in an electrostatic wave propagating nearly perpendicularly to $\boldsymbol{B}_0$ [44, 45]. Stochasticity around the fundamental and first harmonic is also theoretically predicted [46]; attributing the form (84) to the resulting damping, however, is arbitrary although convenient.

In the code separate bookkeeping is made of the power absorbed by this *ad hoc* damping, while ELD of IB waves is obviously attributed to the electron. The sum of these two absorption

terms, in any case, should not be confused with the amount of power mode-converted to IB waves in the first place. Indeed, residual ion cyclotron and electron Landau damping can damp these waves even before they reach the region where either ELD sets in or $\lambda_m > \lambda_{\rm crit}$. In a global code the efficiency of mode conversion cannot be easily 'measured', since it is impossible to split the power flux and the absorbed power density into separate contributions from the individual WKB solutions of the local dispersion relation. It is, nevertheless, usually possible to distinguish qualitatively between the various damping mechanisms from the radial position of the respective absorption peaks.

7.5. Regularization of Alfvén resonances

In the ion cyclotron frequency range Alfvén resonances ($\omega < \Omega_{\rm ci}$) or lower hybrid resonances ($\omega > \Omega_{\rm ci}$)

$$n_\parallel^2 - S \simeq 0 \tag{85}$$

can occur at low density in the plasma periphery. To reduce the numerical problems due to these quasi-singularities of the FLR wave equations, an enhanced 'collisional' damping can be used, by adding to $\hat{S}$ a term of the form

$$\delta\hat{S} = {\rm i}K_{\rm awr}|{\rm Re}\,(R)|\exp\left\{-Q_{\rm awr}^2\frac{(n_\parallel^2 - {\rm Re}\,(S))^2 + {\rm Im}\,(S)^2}{({\rm Re}\,(R))^2}\right\}. \tag{86}$$

The parameters $K_{\rm awr}$ and $Q_{\rm awr}$ can be adjusted by the user; values $K_{\rm awr} \simeq 0.1$ and $Q_{\rm awr} \simeq 10$ usually ensure that damping is localized near the singularity and has a negligible effect on the overall power balance, yet is sufficiently strong to ensure a well behaved solution. In the code separate bookkeeping is made of the amount of damping due to $\delta\hat{S}$. Physically, if power is absorbed by collisional broadening of wave resonances, it should be attributed to the electrons.

8. The order reduction algorithm and other options

The order reduction algorithm (ORA) was introduced in [22] to cure the shortcomings of the zero Larmor radius approximation without renouncing its simplicity. For this purpose, the zero Larmor radius ion current is 'corrected' by adding the appropriate FLR corrections to the dielectric tensor in algebraic instead of differential form.

In TORIC, this is implemented by replacing $\hat{R}$ and $\hat{L}$ (equations (18)) with the quantities

$$\hat{R}_{\rm eff} = \hat{R} - \hat{\rho}^{(2)}n_\perp^2|_{\rm FW} \qquad \hat{L}_{\rm eff} = \hat{L} - \hat{\lambda}^{(2)}n_\perp^2|_{\rm FW} \tag{87}$$

where $\hat{\rho}^{(2)}$ and $\hat{\lambda}^{(2)}$ are given by equation (24), and $n_\perp^2|_{\rm FW}$ is the perpendicular index of the compressional wave, obtained by solving the local WKB dispersion relation including FLR corrections. In the limit of negligible electron inertia, which is sufficient for the fast wave, this dispersion relation is

$$\sigma^{(2)}n_\perp^4 + ((n_\parallel^2 - \hat{S}) + (n_\parallel^2 - \hat{R})\hat{\lambda}^{(2)} + (n_\parallel^2 - \hat{L})\hat{\rho}^{(2)})n_\perp^2 + (n_\parallel^2 - \hat{L})(n_\parallel^2 - \hat{R}) = 0. \tag{88}$$

Care must be taken to choose the fast wave root throughout: in the evanescence regions between cut off and confluence with the ion Bernstein wave, it is the root with a positive imaginary part. The FLR corrections to $\hat{R}$ and $\hat{L}$ provide the correct amount of damping of the fast wave near first-harmonic cyclotron resonances, and eliminate the singularity of the cold limit at ion–ion resonances. Too sharp ion–ion resonances (in particular when the fundamental of the minority does not coincide with the first harmonic of the majority) can be regularized as described in section 7.5.

Recently Jaeger *et al* [50] made a detailed analysis of the ORA in toroidal geometry, pointing out that there are, in principle, different realizations of this scheme. In our version of the ORA only the ion FLR current is modified by replacing the second-order differential operators with $k_\perp^2$ as discussed earlier. In our opinion, this is the most natural choice, since in the IC frequency range the FLR electron current does not give rise to short-wavelength solutions (as long as their very small contribution to $\sigma^{(2)}$ is neglected). There is, therefore, no advantage in performing the same substitution in electron terms, which, moreover, depend on the *a priori* unknown direction of $\boldsymbol{k}_\perp$. To avoid misunderstandings, let us stress that, if the poloidal component of the static magnetic field is taken into account, the ORA is not completely free from short-wavelength features: near ion-hybrid and Alfvén resonances the compressional wave can mode-convert directly to the shear Alfvèn wave. This feature is not specific of the ORA, but, rather, is characteristic of the cold-plasma (zero Larmor radius) approximation, and is non-physical unless the plasma pressure is so low that $\beta \ll m_e/m_i$, a condition which is practically never satisfied in tokamak plasmas. The FLR effects euristically included in the ORA to some extent reduce the non-physical excitation of the shear wave; it is nevertheless generally safer to neglect the poloidal component of the static magnetic field when using the ORA.

A number of additional options has been incorporated in TORIC, either to allow comparison with simpler approximations, or to improve modelling, particularly of outer plasma layers. In the first group, it is possible to omit, separately or simultaneously: the parallel electric field in the plasma, $E_\zeta = 0$; the broadening of ion cyclotron resonances due to toroidicity; the poloidal component of the confining magnetic field; and the finite Larmor radius contributions to the ion and electron HF currents. In the second group the most important option is the possibility of assuming that a tenuous, cold plasma extends up to the wall, whose density can also be modulated in ϑ to make it vanish in the antenna region. In the interest of brevity, however, we will not discuss these options further.

9. Radial discretization and numerical implementation

9.1. Implementation of the spectral representation

As mentioned earlier, the spectral ansatz (47) together with the approximations to the toroidal plasma dispersion function discussed in section 5 transforms the integrodifferential FLR wave equations into a system of coupled ordinary differential equations in the radial variable ψ, whose coefficients are evaluated using the fast Fourier transform (FFT). For optimal efficiency of the FFT the number M_c of poloidal Fourier components used in the representation of the coefficients is always a power of two. The number $M_s = 2M_{max}+1$ of poloidal modes kept in the representation of the solution, on the other hand, is always odd, so that $-M_{max} \leqslant m \leqslant M_{max}$. To avoid having to check the summation boundaries in the convolutions between coefficients and unknowns, and to make optimal use of the information about ϑ dependence of the coefficients, the condition $M_c > 2M_{max}$ is imposed. To reconstruct the fields after solution of the radial equations the inverse Fourier transform must be taken. To be able to use the same FFT routine as for the evaluation of the coefficients, the arrays of field components on each magnetic surface are extended to M_c elements by adding zeros in the outer positions.

Construction of the FFT of order M_c requires information from M_c equally spaced points in ϑ. From this obvious statement it becomes clear that M_c must be sufficient to allow a good resolution of the poloidal variation of the resonant Z-functions on each magnetic surface, while M_s must be sufficient to resolve numerically the shortest wavelength waves occurring in the solution. To some extent these two criteria are independent from each other; it is nevertheless clear that the most reasonable choice of M_c is the smallest power of two greater than 2 M_s.

9.2. The radial discretization

To implement the finite element (FEM) discretization, the interval $0 \leqslant \psi \leqslant 1$ is subdivided into $N_{\rm p}$ intervals (*elements*), and the solution is assumed to have the form

$$E_\alpha^m(\psi) = \sum_r \sum_{\nu=1}^{2} E_{\alpha,\nu}^m(r)\hat{H}_{r,\nu}(\xi_r) \tag{89}$$

where ξ_r ($-1 \leqslant \xi_{\rm i} \leqslant 1$) is the normalized coordinate on element r, and the support functions $\hat{H}_{r,\nu}(\xi_r)$ are

$$\begin{aligned} \hat{H}_{r,0}(\xi_r) &= H_0(\xi) \qquad -1 \leqslant \xi \leqslant 1 \\ \hat{H}_{r,1}(\xi_r) &= \begin{cases} (\psi_{r+1} - \psi_r)H_1(\xi) & \text{if } 0 \leqslant \xi \leqslant 1 \\ (\psi_r - \psi_{r-1})H_1(\xi) & \text{if } (-1 \leqslant \xi \leqslant 0) \end{cases} \end{aligned} \tag{90}$$

in terms of the Hermite cubic interpolating polynomials H_0 and H_1, defined on the master interval $-1 \leqslant \xi \leqslant +1$ as

$$\begin{aligned} H_0(\xi) &= (|\xi| - 1)^2(2|\xi| + 1) \\ H_1(\xi) &= (|\xi| - 1)^2\xi. \end{aligned} \tag{91}$$

With these normalizations, $E_\alpha^0(r)$ and $E_\alpha^1(r)$ are the values of E_α and of its first derivative, respectively, at the mesh point $\psi = \psi_r$. Cubic Hermite FEM have the distinctive advantage of allowing solutions (wave electric field) with continuous derivative (wave magnetic field) everywhere. They were introduced for wave problems in [21].

9.3. The solver

The discretized system has a block structure

$$\mathbf{L}_i \cdot \boldsymbol{x}_{i-1} + \mathbf{D}_i \cdot \boldsymbol{x}_i + \mathbf{R}_i \cdot \boldsymbol{x}_{i+1} = \boldsymbol{y}_i \qquad i = 1, \ldots, N_{\rm p} \tag{92}$$

with

$$\mathbf{L}_1 = 0 \qquad \mathbf{R}_{N_{\rm p}} = 0. \tag{93}$$

Each $\boldsymbol{x}_i$ is a (6 $M_{\rm s}$)-dimensional complex vector made up of the Fourier components of $\boldsymbol{E}$ and $\mathrm{d}\boldsymbol{E}/\mathrm{d}\psi$ at $\psi = \psi_i$. Adding boundary conditions at the plasma edge and at the antenna increases the number of elements by two, but does not alter this structure; the antenna current contributes to $\boldsymbol{y}_i$ at ψ_A. The other boundary conditions are easily implemented by modifying the appropriate blocks of coefficients.

The ansatz

$$\boldsymbol{x}_{i-1} = \mathbf{E}_{i-1} \cdot \boldsymbol{x}_i + \boldsymbol{F}_{i-1} \tag{94}$$

leads to the upward recursive relation

$$\begin{aligned} \mathbf{E}_i &= -(\mathbf{D}_i + \mathbf{L}_i \cdot \mathbf{E}_{i-1})^{-1} \cdot \mathbf{R}_i \\ \boldsymbol{F}_i &= (\mathbf{D}_i + \mathbf{L}_i \cdot \mathbf{E}_{i-1})^{-1} \cdot (\boldsymbol{y}_i - \mathbf{L}_i \cdot \boldsymbol{F}_{i-1}) \end{aligned} \tag{95}$$

to be initialized by $\mathbf{E}_0 = 0$, $\boldsymbol{F}_0 = 0$. The downward recursion (95) then begins with $\boldsymbol{x}_{N_{\rm p}} = \boldsymbol{F}_{N_{\rm p}}$. The matrices to be inverted are LU-decomposed and the equations (95) are implemented using LINPAK routines. The solver based on this method has the advantage of simplicity and is relatively efficient, but is very memory-consuming: for $M_{\rm s}$ poloidal modes and N_ψ radial points ($(6 \times M_{\rm s})^2 \times N_\psi$) complex elements need to be stored. The size of the corresponding arrays limits the largest mesh which can be handled in a given computer.

9.4. Accuracy and convergence

It is difficult to validate rigorously a code like TORIC, since no analytic solution of the IC wave equations in tokamaks is known. To test the code, one can check the consistency of the power balance, and compare runs with increasingly finer mesh. Most importantly, one should systematically check the results of TORIC with the expectations from the physics of IC waves propagation and absorption. For this purpose, a useful tool is the code FELICE, which solves the same set of equations as TORIC in plane-stratified geometry (i.e. in a plasma slab with the same parameters as the real plasma along the equatorial plane, and neglecting the poloidal component of the static magnetic field). FELICE is much faster, and can use a much finer mesh to ensure good resolution of short wavelength features, but cannot provide reliable power deposition profiles. Comparison of TORIC with FELICE also allows us to identify specifically toroidal effects.

The resistive load $P_{\mathrm{ant}} = 0.5\ \mathrm{Re}\,(\boldsymbol{J}_{\mathrm{A}} \cdot \boldsymbol{E})$ and the power flux P_{em} through the plasma surface evaluated by TORIC usually agree very well (better than one part in a thousand). Even in runs with acceptable results, on the other hand, the total power P_{abs} deposited in the plasma can differ from P_{ant} and P_{em} by an amount between 0.5% and several per cent. This is due, in part, to the additional integrations required to evaluate P_{abs}. Inaccuracies due to the essential boundary conditions at the plasma surface, and to a lesser extent at the Faraday screen and the antenna, however, are likely to contribute as well. This is suggested, in particular, by the fact that in situations in which the power absorption per transit is expected to be poor the agreement between P_{abs} and P_{ant} is often less satisfactory than in scenarios with good absorption. In the experiments, poor absorption in the plasma core enhances parasitic effects near the surface, including the production of impurities [47]; in TORIC it amplifies numerical inaccuracies at the most sensitive points of the mesh, which are those corresponding to discontinuities (we recall that in the complete absence of absorption the solution of the wave equations solved by TORIC would diverge).

By far the most common cause of failure of TORIC is lack of convergence of the poloidal Fourier representation of the solution. For a medium-size tokamak (ASDEX Upgrade, $R_0 = 1.65$ m, $a = 0.5$ m) 15 or 31 poloidal modes (with 32 or 64 poloidal mesh points, respectively) are usually sufficient. In some scenarios, however, the poloidal variation of the coefficients of the wave equations is too sharp to be represented by a truncated Fourier series with a reasonable number of modes. The most difficult case we have encountered was a hydrogen plasma with a minority of He_3^{++} ions. Since in this scenario IB waves satisfy the small ion Larmor radius condition only marginally even close to the mode conversion layer, it is practically impossible to have a sufficiently fine mesh for their numerical resolution.

10. An example

As an example, we investigated harmonic heating of a deuterium plasma in ASDEX Upgrade [48]. The magnetic configuration was assumed to have ellipticity $\eta(a) = 1.6$ and triangularity $\delta(a) = -0.15$ at the plasma boundary, and a Shafranov shift of 4.5 cm. The magnetic field was taken to be 2.1 Tesla on the magnetic axis, and the total current 0.75 MA. The density had a central value of 6.3×10^{-19} per m^{-3} with a rather flat radial profile, and the temperatures ($T_{\mathrm{e}} = T_{\mathrm{i}}$) reached 4 keV in the centre, with nearly triangular profiles. The high central temperature is typical of discharges preheated by neutral beam injection.

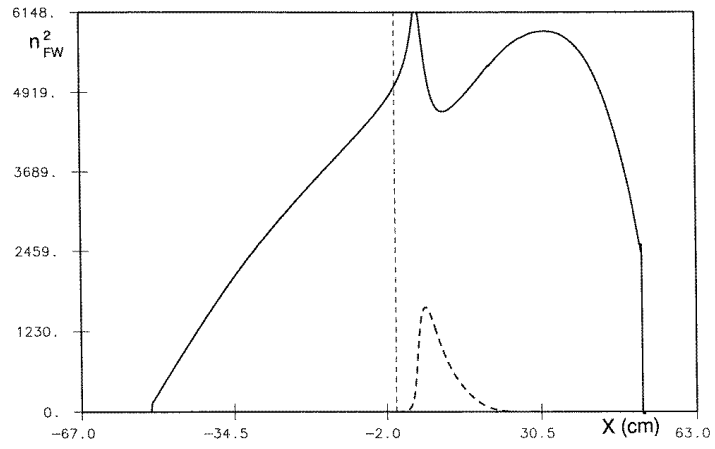

(a)

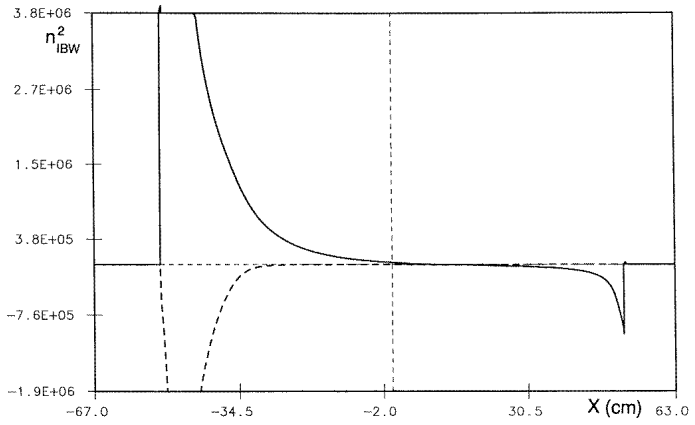

(b)

Figure 1. Perpendicular index squared along the equatorial plane of ASDEX Upgrade, for the toroidal mode $n_\varphi = 12$ with $m = 0$: (a) fast wave; (b) ion Bernstein wave (full curve, real part; broken curve, imaginary part).

10.1. Diagnostic tools

TORIC offers a number of diagnostic tools which can be used to understand the physics of a particular IC scenario before solving Maxwell equations. Here we show, for the mode $n_\varphi = 12$ with $m = 0$, along the equatorial plane: the perpendicular index of the fast and the IB waves (figures 1(a) and (b)); the values of $\lambda^{(2)}$ and $\rho^{(2)}$ (figure 2); and the quantities $\delta\sigma^{(2)}$ which are added to $\sigma^{(2)} = (\lambda^{(2)} + \rho^{(2)})/2$ to take into account ELD and stochastic ion damping (figure 3). Because of the flat density profile with high density up to the Faraday screen, the low-density R cut off is outside the plasma. We also note that the imaginary part of $n^2_\perp|_{\mathrm{FW}}$ in the vicinity of $\omega = 2\Omega_{\mathrm{D}}$ (which is located 11.3 cm to the low-field side of the magnetic axis) is mostly due to the evanesce layer between the cyclotron harmonic resonance and the confluence with the IB branch [49], rather than to IC absorption. In this region the two roots are approximately complex conjugate, $\mathrm{Im}\,(n^2_\perp)_{\mathrm{BW}} \simeq -\mathrm{Im}\,(n^2_\perp)_{\mathrm{FW}}$, but this is not visible in figure 1 because of

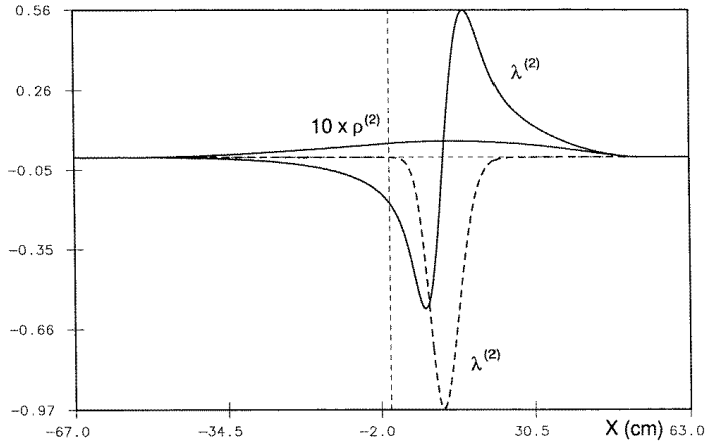

Figure 2. The coefficients $\lambda^{(2)}$ (full curve, real part; broken curve, imaginary part) and $\rho(2)$ (purely real; multiplied by 10 to make it visible on the same scale) along the equatorial plane.

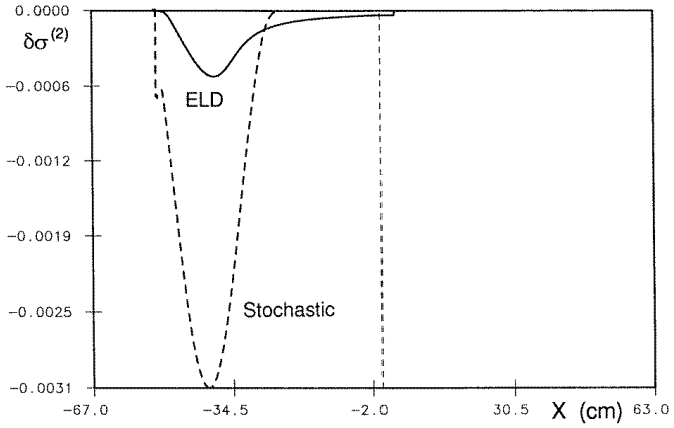

Figure 3. The correction $\delta\sigma(2)$ due to electron Landau damping (full curve) and stochastic ion damping (with $K_1 = K_2 = \tilde{\lambda}_{\text{crit}} = 1$, broken curve) along the equatorial plane.

the widely different vertical scale. The optical thickness of the evanescence region, however, is appreciably smaller than unity ($\eta \simeq 0.07$), and, therefore, we do not expect a large standing wave ratio between the antenna and this layer. The contribution of cyclotron harmonic damping to the imaginary part of $\lambda^{(2)}$ is visible in figure 2; by comparison, the two contributions to $\delta\sigma^{(2)}$ are quite small. Stochastic ion damping is assumed to set in more than 25 cm to the HF side of the mode-conversion layer; nevertheless, assuming the threshold condition to be $k_\perp \rho_{\text{i}} \geqslant 1$, it peaks only slightly to the outside of the ELD contribution. The (negative) imaginary part of $n_\perp^2|_{\text{IBW}}$ due to ELD and stochastic damping is visible in figure 1(b) close to the inner plasma edge.

Also interesting are the local values of $k_\parallel^{mn_\varphi}$ and the corresponding values of $x_{0\text{e}} = \omega/k_\parallel v_{\text{the}}$ along the equatorial plane, which are shown in figure 4, again for $n_\varphi = 12$, and $m = 0, \pm 7$ (the typical range of m values in the centre of the plasma). These figures give an idea of

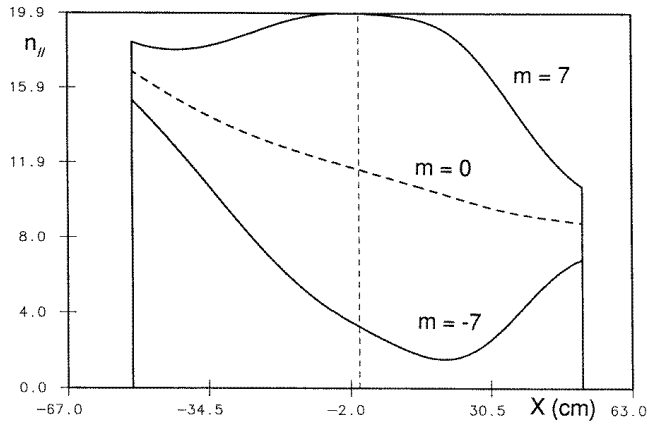

(a)

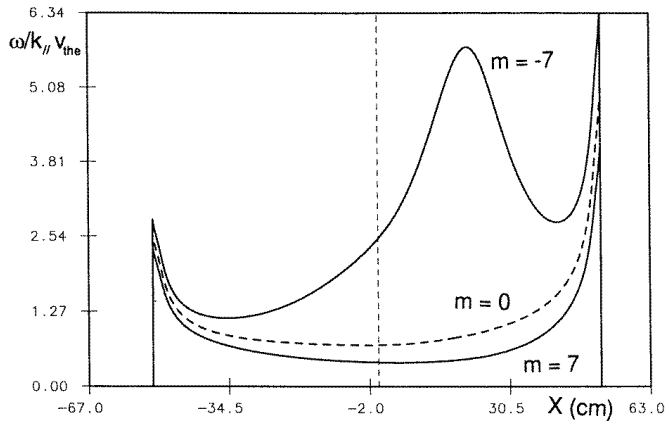

(b)

Figure 4. (a) Local values of $k_{\parallel}^{mn}$ for $n_\varphi = 12$ and $m = 0$ (broken curve) and $m = \pm 7$ (full curves) along the equatorial plane. (b) Local values of $x_{0e} = \omega / k_{\parallel}^{mn} v_{the}$ for $n_\varphi = 12$ and the same values of m.

the $k_\parallel$-spectral broadening due to the poloidal component of the static magnetic field. From inspection of these figures, for example, one immediately concludes that taking this effect into account is essential to evaluate correctly the quasilinear velocity-space diffusion coefficient for fast wave current drive [20]. In the present case, the Fourier components with large negative m will suffer only a weak ELD in the outer half of the plasma, in spite of the fact that for $m = 0$ the parallel phase velocity is of the order of the electron thermal velocity over most of the plasma cross section.

10.2. Field pattern and power deposition profiles

In figure 5 we show contour plots of the real part of the three components $E_\pm$, $E_\parallel$ of the wave electric field in the poloidal cross section for the toroidal mode $n_\varphi = 12$. Here 31 poloidal modes were used (64 points in the poloidal angle ϑ). Only the field inside the plasma is shown: the electric field in the vacuum layer is appreciably larger, and would be the dominant feature

if also plotted. The compressional wave is easily recognized between the antenna and the plasma centre in all the components. The IB wave, on the other hand, is clearly visible to the left of the centre only in E_+, and to a lesser extent in E_ζ. This is easily understood by noting that for the fast wave $|E_+/E_-| \sim |\hat{R}/\hat{L}| \ll 1$; the IB wave, by contrast, is linearly polarized, and its amplitude is comparable to $E_+|_{\mathrm{FW}}$, hence much smaller than $E_-|_{\mathrm{FW}}$. The parallel field is small for both waves (for a current of 1 A in the antenna, the maximum amplitude of E_-, E_+, and E_ζ, in the plasma are 9.7 V m^{-1}, 2.3 V m^{-1}, and 0.01 V m^{-1}, respectively).

Figure 6 shows the power deposition profiles. Globally, 67.1% of the power is deposited in deuterium by harmonic cyclotron damping, 12.45% in the electrons, mainly through the IB waves, and the remaining 20.45% are absorbed via stochastic damping of the IB waves. The broad, somewhat off-axis, peak of harmonic cyclotron heating is due to the finite vertical extent of the large-field region, and is much larger than the Doppler width of the cyclotron layer, even taking toroidal broadening into account. Electron Landau damping and stochastic damping give rise to even broader deposition profiles; the latter, in addition, is peaked well outside the others, so that the corresponding power density is low due to the large specific volume at this radius.

By plotting the coefficients E_ψ^m against m at different values of ψ (figure 7) the convergence of the poloidal Fourier expansion can be tested. In this case 31 poloidal modes are enough for $\psi \lesssim 0.6$, but clearly insufficient outside this radius. The results, fortunately, appear to be relatively robust against such a lack of numerical resolution in the outer domain, as long as IB waves are mostly absorbed in the inner region. On the one hand, the total absorbed power agrees within 0.5% with the power radiated by the antenna. On the other hand, if the number of poloidal Fourier components is halved, so that good convergence is further restricted to $\psi \lesssim 0.4$, the field distribution patterns, the power deposition profiles and the global power balance, are not greatly altered. In the contour plot of $\mathrm{Re}\,(E_+)$ in the poloidal cross section (figure 8) the compressional wave shows more up-down asymmetry than in figure 5(a), while IB waves have a somewhat larger relative amplitude, but tend to follow more closely the magnetic surfaces, a consequence of the reduced numerical resolution in the poloidal direction. To the same cause one can attribute the fact that the power distribution profiles are slightly more peaked (figure 9). The global distribution of power between the various channels (62.3% to deuterium, 13.7% to the electrons, and 24% to stochastic ion damping) is very similar to the previous case.

10.3. Results of the order reduction algorithm

Figure 10 is a contour plot of $\mathrm{Re}\,(E_\psi)$ in the poloidal plane evaluated with the ORA for the same plasma parameters and, again, $n_\varphi = 12$; figure 11 shows the corresponding power deposition profiles. In this case 15 poloidal Fourier components (32 mesh points in ϑ) and 200 radial points were used: the execution time was a factor $\sim$15 shorter than in the case of figure 5, and a factor $\sim$4 than in the case of figure 8. One could decrease somewhat the number of radial points without spoiling the results, but halving the number of poloidal components (which would result in a further reduction of the execution time by a factor of $\sim$4) appears to be incompatible with acceptable convergence.

The field pattern of the fast wave is nearly identical to the previous case, including the up-down asymmetry and the position of individual wavefronts. The elimination of mode conversion, however, allows stronger focussing near the magnetic axis. As a consequence, the profile of power deposition to the deututerons is appreciably narrower. The global repartition of the power is 82.25% to the ions and 16.75% to the electrons.

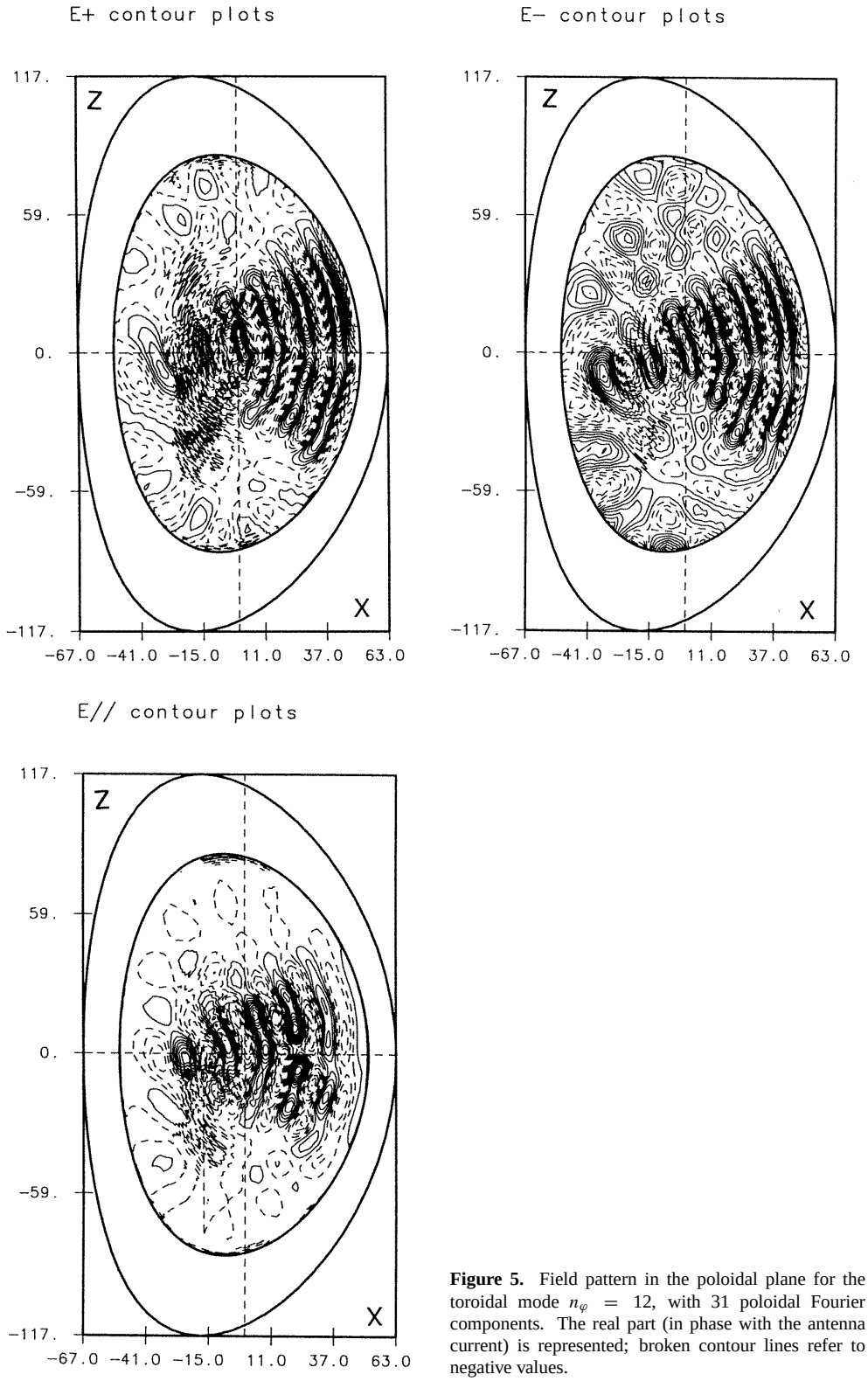

Figure 5. Field pattern in the poloidal plane for the toroidal mode $n_\varphi = 12$, with 31 poloidal Fourier components. The real part (in phase with the antenna current) is represented; broken contour lines refer to negative values.

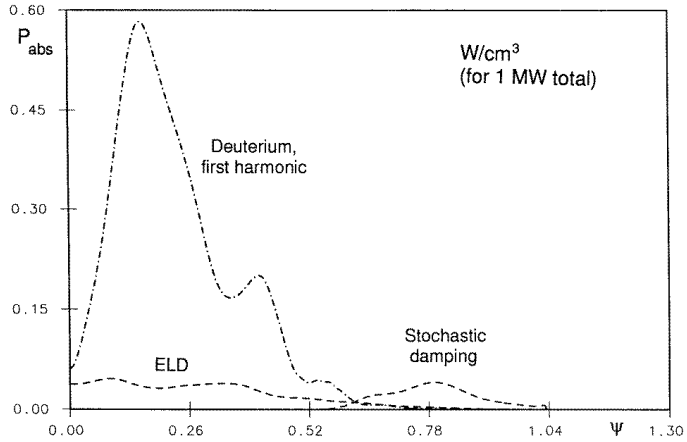

Figure 6. Power deposition profiles for the toroidal mode $n_\varphi = 12$, with 31 poloidal Fourier components.

10.4. Toroidal wavenumber scan

It is clear that a satisfactory test of the code and a reliable comparison of different approximations cannot be made on the basis of a single case. We have, therefore, made a series of runs varying the toroidal mode number n_φ, while keeping all other parameters constant. In TORIC 15 poloidal components (32 poloidal points) were used for this scan. In figure 12 we compare the fraction of power deposited in the different absorption channels according to TORIC, to FELICE, and to TORIC with the ORA option as functions of n_φ. The fraction of power deposited in the various channels is remarkably similar in the three cases, but there are also significant differences.

At low values of n_φ ($n_\varphi \lesssim 10$), in particular, the fraction of power absorbed by the deuterons approaches zero according to FELICE, and unity in the ORA approximation. The full TORIC predictions are closer to those of the ORA approximation, reaching about 0.8 at $n_\varphi = 0$. The result of FELICE is a spurious feature of the plane-stratified model: in this geometry the imaginary part of the plasma dispersion function which describes cyclotron damping appears numerically to approach zero everywhere as $n_\varphi \to 0$, while in reality it should become proportional to a delta function

$$-x_0\, Z(x_n) \to \frac{\omega}{\omega - n\Omega_c} - \mathrm{i}\pi\,\delta\left(\frac{\omega - n\Omega_c}{\omega}\right) \qquad \text{for } k_\parallel v_{th} \to 0 \qquad (n \geqslant 1). \tag{96}$$

The delta-function behaviour, on the other hand, is automatically picked up in TORIC by the toroidal correction to $k_\parallel$ discussed in section 5.3.

The predicted efficiencies of ELD agree well over the whole range. A closer look, however, shows that both FELICE and the ORA approximation predict ELD to vanish exponentially as $n_\varphi \to 0$, while according to the full TORIC code it remains finite, although small, even at $n_\varphi = 0$. This is due to the broadening of the effective $k_\parallel$-spectrum by the poloidal wavenumber m in the presence of the poloidal static magnetic field B_{pol}. In principle, this effect could be taken into account also in the ORA; if $B_{pol} \neq 0$, however, runs for toroidal modes with low n_φ in the ORA approximation are plagued by spurious excitation of the shear Alfvén wave, and, therefore, do not give reliable results.

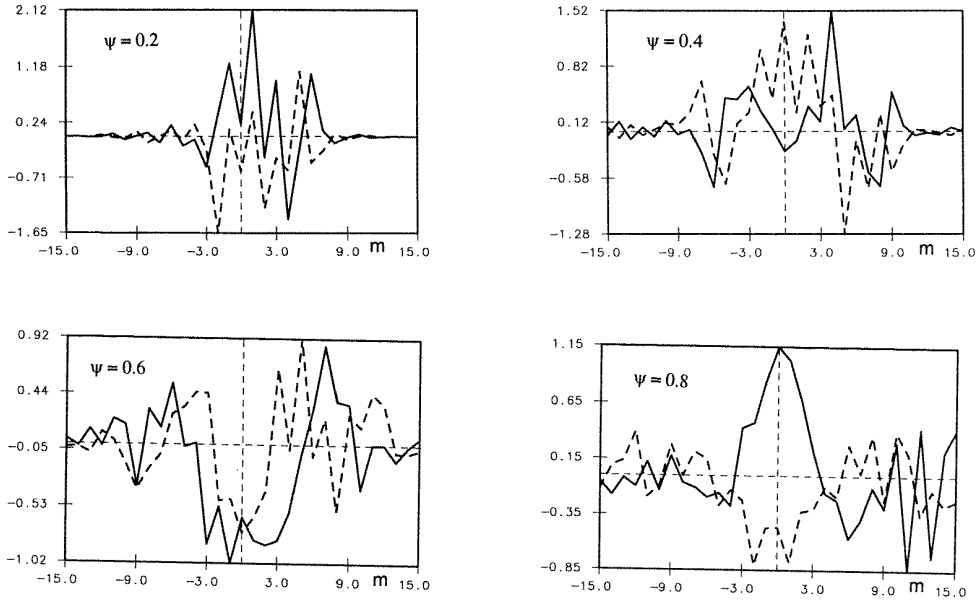

Figure 7. Coefficients of the poloidal Fourier expansion of E_ψ at four radial positions.

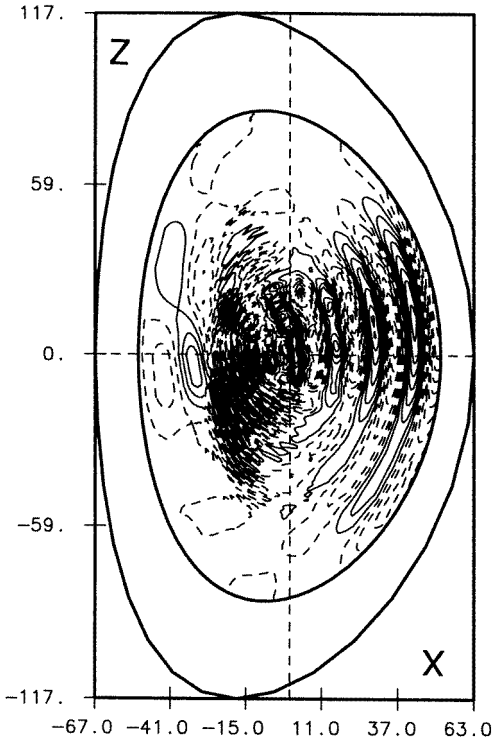

Figure 8. Contour plot of $\mathrm{Re}\,(E_\psi)$ in the poloidal cross section with 15 poloidal Fourier components.

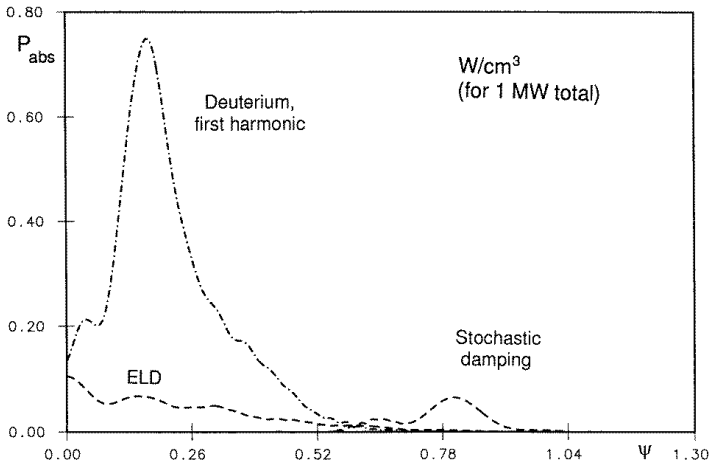

Figure 9. Power deposition profiles for the toroidal mode $n_\varphi = 12$, with 15 poloidal Fourier components.

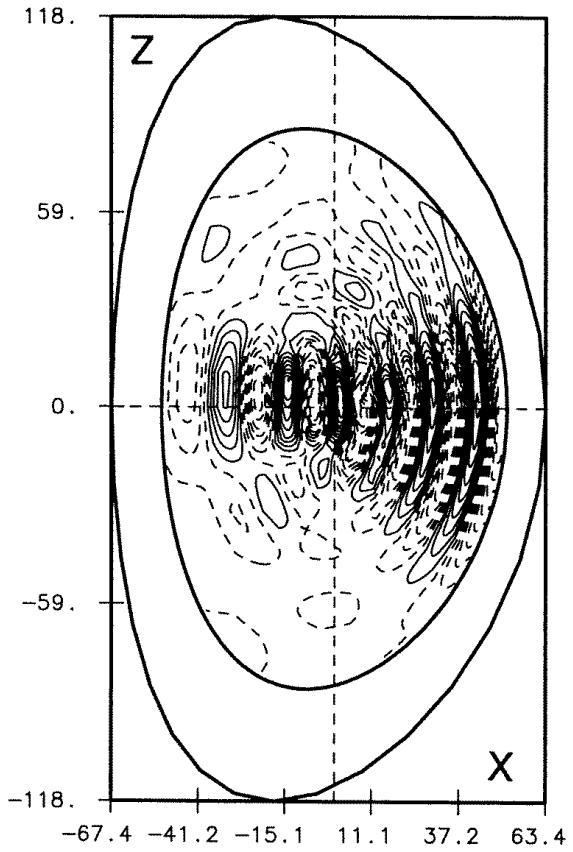

Figure 10. Contour plot of Re (E_ψ) in the poloidal cross section; order reduction algorithm with 200 radial points and 15 poloidal Fourier components.

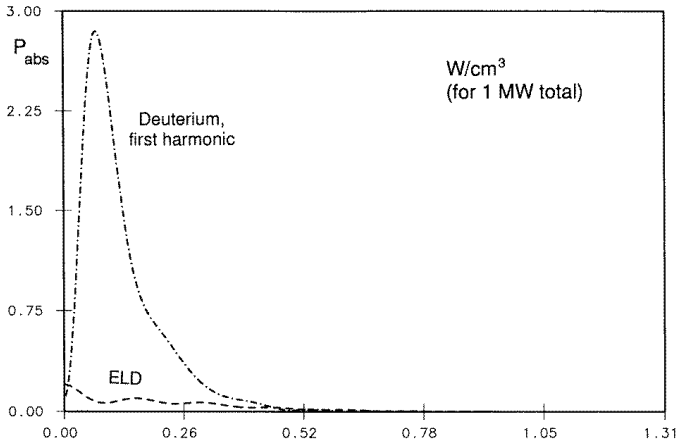

Figure 11. Power deposition profiles for the toroidal mode $n_\varphi = 12$; order reduction algorithm with 200 radial points and 15 poloidal Fourier components.

As mentioned in section 7.4, the region of efficient ELD is not fully opaque to IB waves, and additional 'stochastic damping' is required to absorb these waves when $k_\perp|_{\mathrm{IBW}}\rho_\mathrm{i} \gtrsim 1$. In the present case it was necessary to take $K_1 = 25$ in equation (84) to obtain satisfactory results. The amount of power dissipated in this way approaches 100% in FELICE when $n_\varphi \to 0$, since, in plane stratified geometry, this is the only dissipative mechanism which does not vanish in this limit. In TORIC, by contrast, it remains more reasonably of the order of 20%. While according to FELICE it decreases rapidly with increasing toroidal mode number, however, it remains relatively constant up to much larger values of n_φ according to TORIC (in the ORA approximation this absorption channel is, obviously, absent). This occurs primarily at the expense of harmonic cyclotron heating of the deuterons, suggesting that most of the discrepancy might be due to the fact that FELICE takes into account only the conditions in the equatorial plane, where this absorption mechanism (which is proportional to the normalized plasma pressure β) is most efficient. In part, however, it might be a numerical effect, due to insufficient resolution of the IB waves in the poloidal direction in the region $\psi \gtrsim 0.5$. In a few test runs with 31 poloidal modes (one example being the case $n_\varphi = 12$ presented previously) stochastic damping was slightly lower, although still appreciably larger than according to FELICE.

A real antenna always excites a relatively broad range of toroidal modes simultaneously. The ASDEX Upgrade IC antenna consists of two strips 18 cm wide and separated by 20 cm, excited with opposite phases. The toroidal Fourier spectrum of the current, $J_\mathrm{A}(n_\varphi)$, is therefore antisymmetric, and, at a frequency of 30 Mhz, has the first peak at $n_\varphi \simeq 12$. By convoluting the specific antenna load for each mode (the radiated power for 1 A in the conductors) with $J_\mathrm{A}^2(n_\varphi)$ we have compared the radiated power spectrum predicted by TORIC with that predicted by FELICE (the latter code evaluates the power spectrum and the antenna resistance automatically in a single run). The results are shown in figure 13. Not surprisingly, the spectrum evaluated by FELICE has appreciably more structure than the one obtained from TORIC. In plane-stratified geometry individual poloidal modes can be eigenmodes, and can be selectively excited if the single-pass damping is weak enough (in the present scenario damping might be described as 'moderate': single modes are obviously visible, but the overall shape of the spectrum is nevertheless determined by the shape of $J_\mathrm{A}^2(n_\varphi)$). In toroidal geometry the poloidal

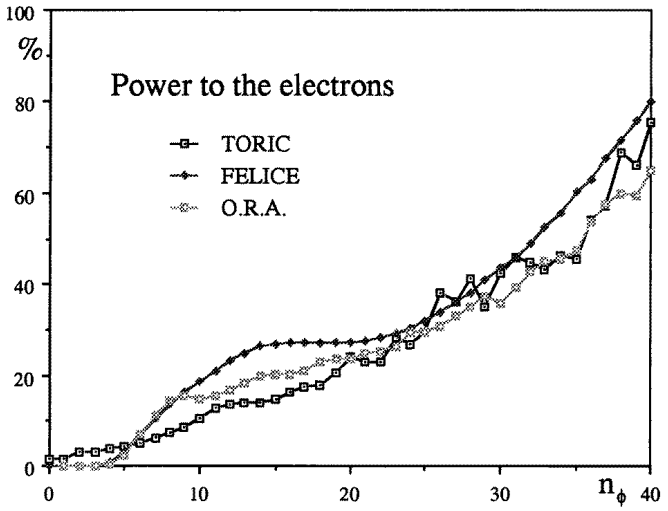

(a)

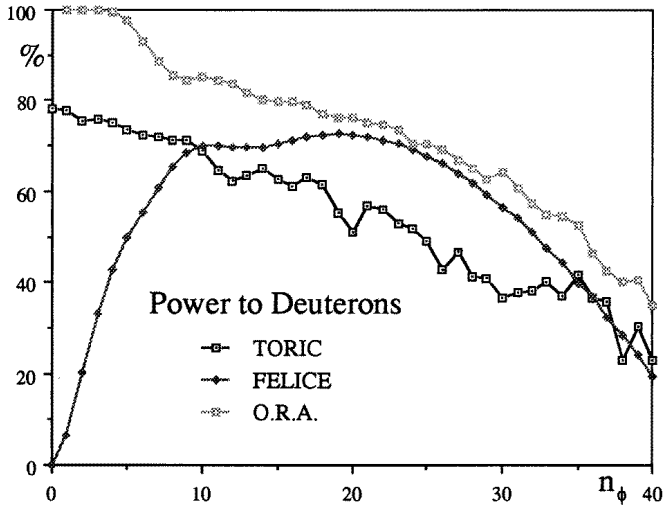

(b)

Figure 12. Fraction of the launced power deposited (a) in the electrons, (b) in deuterium, and (c) absorbed by 'stochastic damping' of IB waves, as functions of the toroidal wavenumber n_φ.

inhomogeneity of the propagation conditions provides an efficient smoothing of the excited spectrum by strongly coupling all poloidal modes to each other. The spectrum evaluated with the ORA is intermediate between those of TORIC and FELICE.

11. Conclusions

The TORIC code successfully solves the FLR integro-differential wave equations in the ion cyclotron range of frequencies in toroidal axisymmetric geometry. Its peculiar feature is

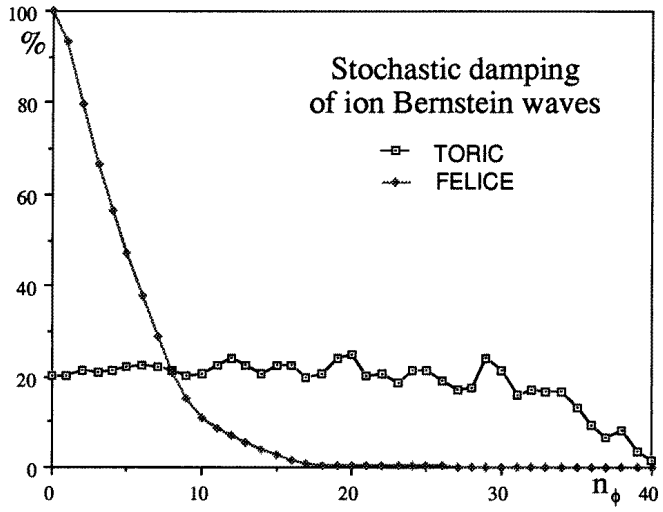

(c)

Figure 12. (Continued)

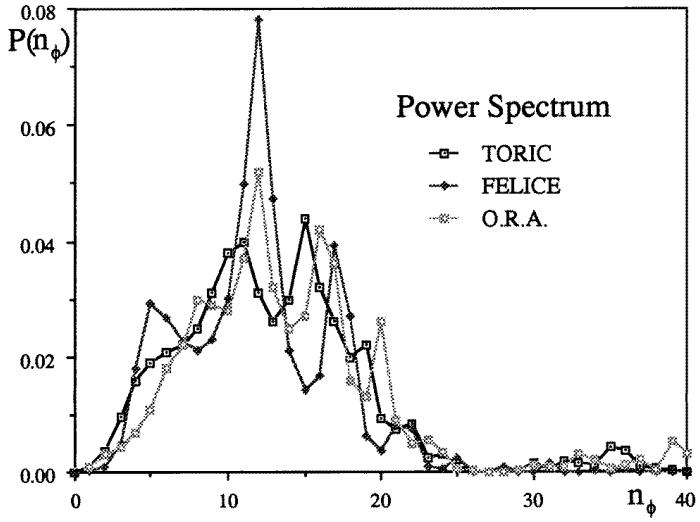

Figure 13. Power spectra (normalized to unity) predicted by TORIC, FELICE, and the ORA approximation for the ASDEX Upgrade antenna.

the ability to describe mode conversion to short-wavelength ion Bernstein waves: although expensive in computing time and memory, this is essential for a full coverage of the physics of ion cyclotron heating and current drive in tokamaks. It allows, in particular, to make detailed comparison with simpler, widely used approximations, such as plane-stratified geometry and the order reduction algorithm. By providing reliable power deposition profiles in most IC heating scenarios, TORIC has proved a useful tool for the interpretation of IC heating experiments [31].

Acknowledgments

Although the code has been largely rewritten, its basic structure is still that of the first version developed in collaboration with Dr T Krücken [10]. Dr P Bonoli and B G Hong have made substantial contributions to debugging and suggested improvements to the code. Useful comments and suggestions from D Batchelor and C S Chiu are also gratefully acknowledged.

References

[1] Fukuyama A, Nishiyama S, Itoh K and Itoh S-I 1983 *Nucl. Fusion* **23** 1005
[2] Appert K, Hellsten T, Vaclavik J and Villard L 1984 *Proc. 4th Int. Symp. on Heating in Toroidal Plasmas (Roma 1984)* vol 1, p 377
[3] Jaeger E F, Batchelor D B and Weitzner H 1988 *Nucl. Fusion* **28** 53
[4] Brambilla M 1989 *Plasma Phys. Control. Fusion* **31** 723
[5] Romero H and Scharer J 1989 *Phys. Fluids* B **1** 252
[6] Stix T H and Swanson D G 1985 *Handbook of Plasma Physics* vol 1, ed A Galeev and R N Sudan (Amsterdam: North-Holland) p 335
[7] Fukuyama A, Itoh K and Itoh S-I 1986 *Comp. Phys. Rep.* **40** 137
[8] Villard L, Appert K, Gruber R and Vaklavik J 1986 *Comp. Phys. Rep.* **40** 95
[9] Edery D and Picq H 1986 *Comput. Phys. Commun.* **4** 95
[10] Brambilla M and Krücken T 1988 *Nucl. Fusion* **28** 1813
[11] Jaeger E F, Batchelor D B, Carter M D and Weitzner H 1990 *Nucl. Fusion* **30** 505
[12] Cattanei G and Murphy A B 1991 *Nucl. Fusion* **31** 219
[13] Jaeger E F, Batchelor D B and Stallings D C 1993 *Nucl. Fusion* **33** 179
[14] Brambilla M 1993 *Plasma Phys. Control. Fusion* **35** A141
[15] Jaun A, Appert K, Vaclavik J and Villard L 1995 *Comput. Phys. Commun.* **92** 153
[16] Stix T H 1975 *Nucl. Fusion* **15** 737
[17] Swanson D G 1981 *Phys. Fluids* **24** 2035
[18] Colestock P L and Kashuba R J 1983 *Nucl. Fusion* **23** 763
[19] Brambilla M 1989 *Plasma Phys. Control. Fusion* **31** 723
[20] Wright J C, Phillips C K and Bonoli P T 1997 *Nucl. Fusion* **37** 1349
[21] Appert K, Hellsten T, Vaclavik J and Villard L 1986 *Comput. Phys. Commun.* **4** 73
[22] Smithe D N, Colestock P L, Kashuba R J and Kammash T 1987 *Nucl. Fusion* **27** 1319
[23] Brunner S and Vaclavik J 1993 *Phys. Fluids* B **5** 1695
[24] Alava M J and Heikkinen J A 1994 *J. Comp. Phys.* **114** 85
[25] Brambilla M and Krücken T 1988 *Plasma Phys. Control. Fusion* **30** 1083
[26] Jiang B-N, Wu J and Povinelli L A 1996 *J. Comp. Phys.* **125** 104
[27] Brambilla M 1995 *Nucl. Fusion* **35** 1265
[28] Brambilla M 1996 A full wave code for ion cyclotron waves in toroidal plasmas *Rep. IBB 5/66, Max-Planck-Institut für Plasmaphysik, Garching (Germany), February 1996* unpublished
[29] Fried B D and Conte S D 1961 *The Plasma Dispersion Function* (New York: Academic)
[30] Kaladze T D and Mikhailowskii A B 1975 *Sov. J. Plasma Phys.* **1** 128
[31] Cattanei G and Croci R 1977 *Nucl. Fusion* **17** 239
[32] Kasilov S V, Pyatak A I and Stepanov K M 1990 *Nucl. Fusion* **30** 2467
[33] Becoulet A, Gambier D J, Rax J-M and Samain A 1989 *Proc. 8th Top. Conf. on Applications of RF Power to Plasmas (Irvine, CA, USA)* (New York: American Institute of Physics) p 197
[34] Itoh S-I, Fukuyama A, Itoh K and Nishikawa K 1985 *J. Phys. Soc. Japan* **54** 1800
[35] Faulkoner D W 1987 *Plasma Phys. Control. Fusion* **29** 433
[36] Smithe D, Colestock P L, Kammash T and Kashuba R J 1988 *Phys. Rev. Lett.* **60** 801
[37] Catto P J and Lashmore-Davies C N 1992 *Europ. Topical Conf. on Radiofrequency Heating and Current Drive of Fusion Devices (Bruxelles 1992)* (Geneva: European Physical Society) p 165
[38] Lamalle P U 1993 *Phys. Lett.* **175A** 45
[39] Lamalle P U 1997 *Plasma Phys. Control. Fusion* **39** 1409
[40] Gambier D J and Samain A 1985 *Nucl. Fusion* **25** 283
[41] Brambilla M 1994 *Phys. Lett.* **188A** 376
[42] Gautschi W 1967 *SIAM Rev.* **9** 24
[43] Brambilla M 1998 *Kinetic Theory of Plasma Waves* (Oxford: Oxford University Press) section 30.4

[44] Karney C F F 1978 *Phys. Fluids* **21** 1584
[45] Karney C F F 1979 *Phys. Fluids* **22** 2188
[46] Lichtemberg A J and Lieberman M A 1992 *Regular and Stochastic Motion* (New York: Springer)
[47] Noterdaeme J-M and Van Oost G 1993 *Plasma Phys. Control. Fusion* **35** 1481
[48] Noterdaeme J M *et al* 1997 *Proc. 16th Conf. on Fusion Energy (Montreal 1996)* (Vienna: IAEA) vol 3, p 335
[49] Weynants R R 1974 *Phys. Rev. Lett.* **33** 78
[50] Jaeger E F, Berry L A and Batchelor D B 1998 *Nucl. Fusion* **38** 437
[51] Bonoli P T *et al* 1997 *Phys. Plasmas* **4** 1774